

Cenozoic Exhumation in the Boise Mountains, Idaho, From New Low Temperature Thermochronology Data

A Thesis

Presented in Partial Fulfillment of the Requirements for the

Degree of Master of Science

with a

Major in Geology

in the

College of Graduate Studies

University of Idaho

by

Wenbo Zhan

Approved by:

Major Professor: Jessica R. Stanley, Ph.D.

Committee Members: Elizabeth Cassel, Ph.D.; Timothy Bartholomaeus, Ph.D.

Department Administrator: Alistair M.S. Smith, Ph.D.

May 2023

Abstract

The modern topography of the Atlanta lobe of the Idaho batholith in the North American Cordillera has been identified as a dissected plateau. The plateau was suggested to exist since late Cretaceous, while the dissection was advocated to take place since late Miocene, associated with unusual regional topographic rejuvenation in a post-orogenic extensional tectonic setting in plate interior. However, the previous evidence supporting the timing and mechanism of the dissection is limited. Spatial variability of multiple aspects exists within the Atlanta lobe. Previous studies identified a Miocene cooling and exhumation signal in the southern Atlanta lobe, but the spatial extent of this signal is unknown. To further reconstruct the exhumation history of the region and investigate the mechanisms that cause the internal variability of the Atlanta lobe, we investigate the area using low temperature thermochronology. We sampled the late Cretaceous and Miocene aged granitoid bedrock along the South Fork Payette River (SFPR) and the Middle Fork Boise River (MFBR) in the Boise Mountains, resulting in three vertical and two horizontal sample transects, a total of 21 new apatite (U-Th)/He (AHe) sample dates and 2 new apatite fission track (AFT) dates from previous samples. The AHe dates range from 29.9 ± 3.1 Ma to 3.9 ± 0.8 Ma, and most cooling dates are Miocene to Pliocene. The two AFT dates are 37.89 ± 4.6 Ma and 40.7 ± 4.72 Ma. The thermal history inverse models from the vertical transects show a two-stage cooling during Eocene-Oligocene and late Miocene–Pliocene, supporting the late Miocene incision. The pattern of cooling dates along the river profiles from the horizontal transects suggests that the incision of modern SFPR and MFBR occurred after the major late Miocene cooling period and has been disrupted by faults. Combining our thermochronology data with other geological evidence, we propose a tectonic model to explain the exhumation history and the variability inside the Atlanta lobe. We suggest the Eocene exhumation was due to extension from over-thickened crust, thermal-dynamic uplift, and potential delamination under the Atlanta lobe due to the influx of hot asthenosphere. The Miocene exhumation could have been driven by thermal-dynamic uplift and/or delamination under the Boise Mountains triggered by the nearby Yellowstone hotspot. The incision of the SFPR and MFBR was likely enhanced by base level drop due to the draining of the paleo-Lake Idaho and disrupted by activity on local Basin and Range faults.

Acknowledgment

I thank Dr. Jessica R. Stanley for taking me as her master's student, leading me to the path of thermochronology, providing all the guidance and support academically and mentally during my research, and generously supporting the research with her startup funding. I thank Dr. Elizabeth Cassel and Dr. Timothy Bartholomaeus for advising me as my thesis committee. I thank the Department of Earth and Spatial Sciences at the University of Idaho for supporting my master's study with a full-time Graduate Teaching Assistantship. I thank Kelsey Wetzel for providing apatite samples for fission track dating for this research and providing valuable apatite He data and mapping shape files for the study area from her previous research to me. I thank Chloë Weeks for helping me collect samples for this research during the field trip in the Boise Mountains and teaching me how to use the crusher, miller, sieve, and the Leica binocular microscope to separate, pick, and pack apatite grains for analysis. I thank Haley Thoresen for training me on how to use the Frantz magnetic separator. I thank Jim MacMillian, Victoria Cross, and Dr. Paul O'Sullivan from GeoSeps Services LLC for providing apatite and zircon mineral separation training for me. In addition, I thank Dr. Paul O'Sullivan for performing apatite fission track dating for this research. I thank CU TRaIL faculties for performing apatite (U-Th)/He dating for this research. I thank Yoram Terleth and Carlos Montejo for their suggestions on Python coding and Inkscape for figures of this thesis. The maps were created using QGIS 3.30.0 (QGIS Development Team, 2023). Figures were created using R (v. 4.0.4, R Core Team, 2021), RStudio (v. 1.3.1, RStudio Team, 2020), and Julia (v. 1.8.5, Bezanson et al., 2017), with R packages of ggplot2 (v. 3.4.2, Wickham, 2016), dplyr (v. 1.1.1, Wickham et al., 2021), and thermochronplotr (v. 0.1.0, Stanley, 2021), and Jupyter notebook (Kluyver et al., 2016) of QTQTPlot (Kalin McDannell, 2022).

Dedication

To my mother, father, and brother.

Table of Contents

Abstract.....	ii
Acknowledgments.....	iii
Dedication.....	iv
List of Tables.....	vii
List of Figures.....	viii
Chapter 1: Introduction.....	1
Chapter 2: Background.....	6
Regional tectonic history.....	6
Geology of the study area.....	8
Previous cooling and exhumation study in the Atlanta lobe.....	9
Chapter 3: Methods.....	12
Sampling strategy.....	12
Apatite (U-Th)/He dating.....	12
Thermal history modeling.....	13
Chapter 4: Results.....	25
South Fork Payette River cooling dates.....	25
Middle Fork Boise River cooling dates.....	26
Inverse modeling results.....	27
Chapter 5: Discussion.....	29
Paleogene to Oligocene Exhumation.....	29
Late Miocene Rejuvenation.....	33
Pliocene to Quaternary River Incision and Basin and Range Faults Disturbance.....	36
Chapter 6: Conclusions.....	39

References..... 41

List of Tables

Table 1 Hypothesis and Tests	5
Table 2 Apatite (U-Th)/He Ddata.....	16
Table 3 Thermal History Modeling Input Table.....	22

List of Figures

Figure 1 Topographic map of Idaho.....	4
Figure 2 Geologic map of the Boise Mountains.....	11
Figure 3 AHe date-eU plots of samples of this study.....	26
Figure 4 AHe date-elevation profiles, HeFTy multi-sample inverse modeling results, and QTQt multi-sample inverse modeling results .	28
Figure 5 Cross section across the southern Atlanta lobe of Idaho batholith illustrating the tectonic model for Cenozoic exhumation at the Boise Mountains based on our AHe and AFT data and other geologic evidence.....	32
Figure 6 AHe date-river profile for samples located at river level and river incision model to explain the AHe date-river profile pattern.	38

Chapter 1: Introduction

The classic mechanism for uplifting topography is crustal thickening correlated to plate collision at convergent plate boundaries. However, there are also examples where topographic uplift occurred in plate interior regions that cannot be explained by the classic theory. Constraining upper crustal cooling using low temperature thermochronology is a powerful method to study the landscape exhumation and burial process; detect extension, uplift, erosion, and river incision signals; investigate lower crust and mantle condition; and verify regional tectonic models (e.g., Ault et al., 2019). Here we investigate an atypical plate interior uplift and exhumation event at the Boise Mountains of the Idaho batholith, USA, by constraining regional cooling history with new apatite (U-Th)/He (AHe) and apatite fission track (AFT) data.

The Idaho batholith is located in the North American Cordillera, a region of intense research interest due to its prolonged and complex tectonic history and diverse mantle-lithosphere geodynamics (e.g., DeCelles, 2004; Kruckenberg et al., 2008; Fuentes et al., 2011; Fuentes et al., 2012; Yonkee & Weil, 2015; Gray et al., 2020). The Idaho batholith is surrounded by a series of geologic features that impact Cordilleran tectonics. It is bounded to the west by the Columbia River Basalt (CRB), the $^{87}\text{Sr}/^{86}\text{Sr}$ 0.706 isopleth representing craton-accreted terrane boundary, and the Western Snake River Plain (WSRP); to the south by the Eastern Snake River Plain (ESRP) and calderas from the Yellowstone hotspot track; and to the east by the Challis volcanic fields and Pioneer Mountains core complex (Figure 1). The Idaho batholith itself is also notable. The modern topography of the Idaho batholith is suggested to be a dissected plateau that was once the extent of Nevadaplano during late Cretaceous-Paleogene (e.g., DeCelles, 2004; Cassel et al., 2018; Wetzel & Stanley 2022). However, the dissection of the plateau is suggested to potentially occur during late Miocene, much later than the formation of the plateau (Larimer et al., 2018; Blackwelder, 1912). River morphology studies even indicated that the dissection was due to a northward tilting uplift of the Atlanta lobe, one of the major magmatic belts of the Idaho batholith (Larimer et al., 2018; Mitchell & Yanites, 2019). Although the Atlanta lobe has a uniform lithology sourced from crustal melts with little temporal variability (Gaschnig et al., 2010), there is significant spatial variability within the belt, between rim and internal, northern and southern Atlanta lobe, suggested by seismic

images, surface GPS velocities, fault patterns, and previous thermochronology studies (e.g., Ruppel, 1982; Sweetkind & Blackwell, 1989; Tikoff et al., 2001; Breckenridge et al., 2003; Roth et al., 2008; Schmandt & Humphrey, 2011; Payne et al., 2012; Tian & Zhao, 2012; McCaffrey et al., 2013; Fayon et al., 2017; Wetzell & Stanley, 2022). If the southern Atlanta lobe had a Miocene rejuvenation, this rejuvenation event would be worth investigating, not only because it occurred far away from the convergent boundary during post-orogenic extension, but also because the mechanisms causing this rejuvenation have the potential to explain the spatial variability within the Atlanta lobe. In addition, because of its location at the junction of multiple tectonic features, the tectonic and topographic history of the Idaho batholith bears on the regional tectonics of the Cordillera. Several geodynamic mechanisms could cause Miocene rock uplift in the Atlanta lobe that would result in different timing and patterns of exhumation in the Boise Mountains (Table 1).

First, rock uplift could have been triggered by the nearby eruption of the CRB which potentially could have caused delamination of a dense eclogite root under the Boise Mountains. The uplift of the Wallowa Mountains to the west of the study region has been proposed to be due to lithospheric delamination (Hales et al., 2005), and the high seismic velocity field under the Wallowa Mountains also extends to beneath the Atlanta lobe, including the Boise Mountains (Roth et al., 2008). If this is the case, we would expect regional uplift and exhumation at ~16 Ma, contemporaneous with the CRB eruption. In addition, the western side of the Atlanta lobe might experience more exhumation compared to the east (Table 1).

Second, the prospective late Miocene uplift could be due to effects from the Yellowstone hotspot. The Yellowstone hotspot has been proposed to be a stationary mantle plume overridden by moving North American Plate, leading to the subsidence of the ESRP and the uplift of the surrounding terrain (Pierce & Morgan, 1992; McQuarrie & Rodgers, 1998). The Twin Falls (active 10.9-8.6 Ma) (Pierce and Morgan, 1992; Bonnicksen et al., 2008) and Picabo (active 10.3-8.2 Ma) (Pierce and Morgan, 1992; Vogl et al., 2014) volcanic fields, located just south of the Boise Mountains (Figure 1) is considered part of the track of the Yellowstone hotspot and the plume is inferred to have been beneath these volcanic fields during their active periods. Miocene exhumation observed in the Pioneer Mountains is attributed to a combination of thermal-dynamic and flexural uplift effects as the Yellowstone hotspot passed by (Vogl et

al., 2014). In addition, Larimer et al. (2018) attributed the northward tilting of the central Idaho mountains to delamination under the Boise Mountains triggered by the hotspot. Similarly, we hypothesize that the hot plume can lead to thermal-dynamic uplift and/or delamination under the Boise Mountains when the Twin Falls and Picabo volcanic fields were active. If this is the case, the uplift-triggered exhumation should be at ~ 11 -8 Ma, and we might expect more exhumation to the south closer to the hotspot (Table 1).

Exhumation and dissection of the Plateau could also have occurred in the absence of regional uplift due to extensional processes. Basin and Range faults that started in central Idaho at ~ 17 Ma continue to present day (Dickinson, 2004; Janecke, 1992; Yonkee and Weil, 2015). If extensional faulting is driving exhumation, we should see exhumation adjacent to faults with high offset in the region during the period from ~ 17 Ma to present. Additionally, rivers in the Boise Mountains drain into the WSRP, which is proposed to start extending and subsiding at ~ 16 Ma and accelerate from 12-8.5 Ma (Wetzel & Stanley, 2022, Wood & Clemens, 2002). The WSRP was occupied by paleo-Lake Idaho which drained at ~ 4 Ma (Wood & Clemens, 2002). Both subsidence of the basin and the draining of the lake would lead to a base-level drop and could trigger/enhance river incision in the Boise Mountains (Sweetkind and Blackwell, 1989; Larimer et al., 2019; Mitchell & Yanites, 2019; Wetzel and Stanley, 2022). If these processes were driving exhumation, we should see river incision periods at 16-8 Ma and/or post-4 Ma (Table 1).

To distinguish the mechanism(s) driving landscape rejuvenation in the Boise Mountains, better constraints on the timing and patterns of exhumation are needed. Previous application of low temperature thermochronology to constrain young cooling events in the Atlanta lobe, especially AHe data, was very limited, despite that AHe system has low temperature sensitivity, which may allow it to detect small magnitude, more recent cooling events. Among them, there were only 5 AHe samples with Miocene ages, all at the downstream of the MFBR in the Boise Mountains. Due to the limited spatial extent of these Miocene data, we collected more AHe samples in order to see how extensive this Miocene cooling signal is and to better constrain the timing of the exhumation. Here we present new AHe and AFT data from the Boise Mountains to constrain the timing, pattern, rate, and magnitude of the exhumation and reconstruct topographic evolution history of the region. Combined with other geologic

evidence from previous studies, we can evaluate the regional tectonic history and geodynamic mechanisms driving landscape change.

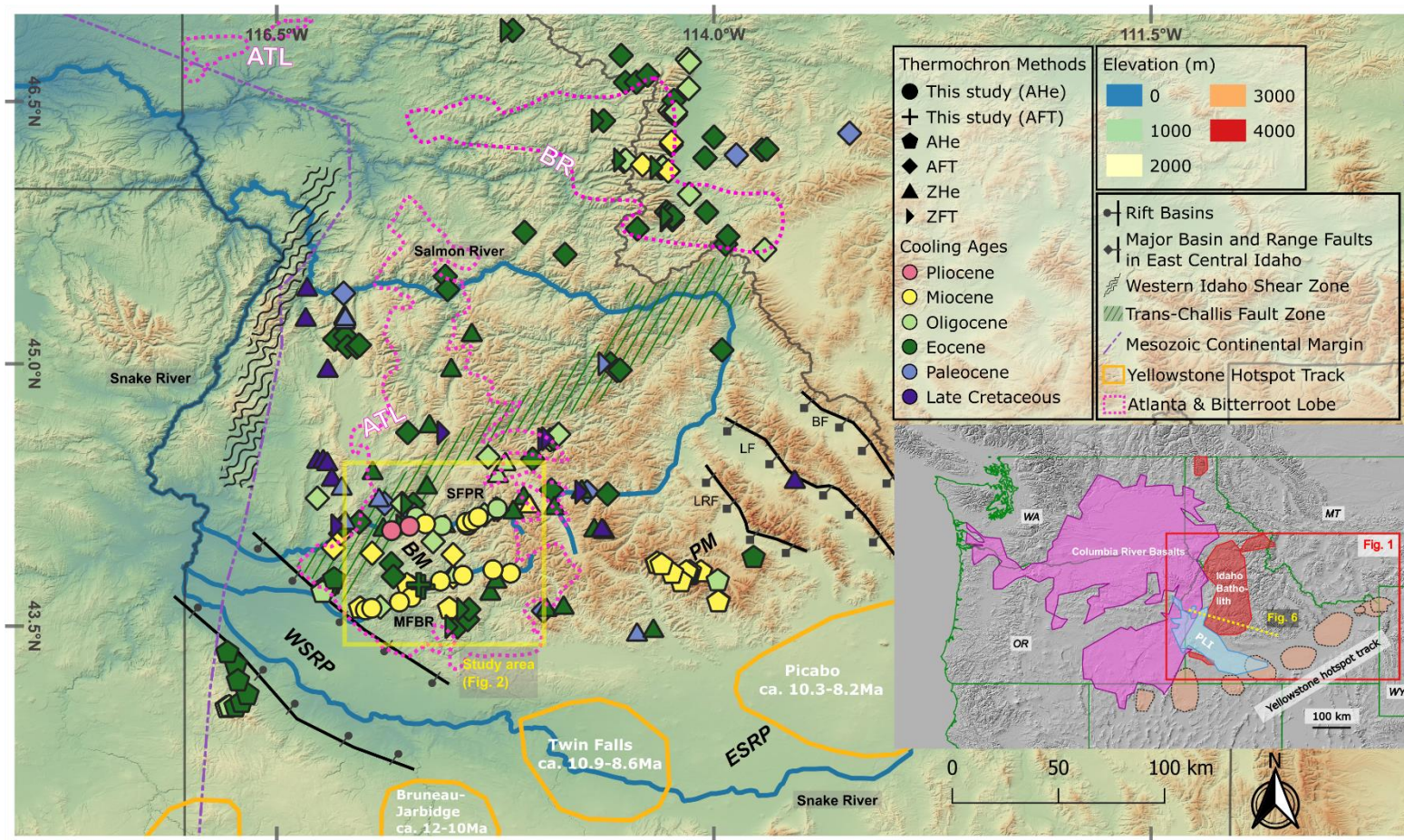


Figure 1. Topographic map of Idaho. Published sample locations and cooling ages from previous thermochronology studies around the Idaho batholith are plotted. (Sweetkind and Blackwell, 1989; Foster and Raza, 2002; Giorgis et al., 2008; Vogl et al., 2014; Fayon et al., 2017; Wetzel and Stanley, 2022). Approximate locations of major geologic features are also highlighted. Names of major rivers and adjacent Yellowstone volcanic centers are labeled. The pale-yellow box outlines the main study area in Figure 2. The inset figure demonstrates regional Pacific NW topography and the approximate location of the Idaho batholith (red), the Columbia the River Basalt (purple), volcanic fields along the Yellowstone hotspot track (tan), and the paleo-Lake Idaho (blue). The red box outlines the area in Figure 1. The Yellow dashed line represents the transect of Figure 6. ATL-Atlanta lobe; BR-Bitterroot lobe; BM-Boise Mountains; PM-Pioneer Mountains; WSRP-Western Snake River Plain; ESRP-Eastern Snake River Plain; SFPR-South Fork Payette River; MFBR-Middle Fork Boise River; LRF-Lost River fault; LF-Lemhi fault; BF-Beaverhead fault; AHe/ZHe-apatite/zircon (U-Th)/He; AFT/ZFT-apatite/zircon fission track. Figure 1 is modified from Wetzel and Stanley (2022). The inset figure is modified from Camp (2013) and Wetzel and Stanley (2022).

Table 1. Hypothesis and Tests

Cause of rapid Exhumation	Expected AHe date feature
(1). Delamination under the Boise Mountains during the peak eruption of the CRB	Regional uplift at the Boise Mountains and associated exhumation and cooling from ~16 Ma; exhumation might be stronger to the west
(2). Thermal dynamic uplift and/or delamination caused by the yellowstone hotspot	Regional uplift at the Boise Mountains and associated exhumation and cooling from ~11-8 Ma; exhumation might be stronger to the south
(3). Basin & Range normal faults	Exhumation adjacent to faults with high offset in the region during the period from ~17 Ma to present
(4). Base level drop caused by subsidence and extension of WSRP and/or draining of the Paleo Lake Idaho	Exhumation adjacent to rivers. River incision period matches major exhumation and cooling window. Incision period during 16-8 Ma and/or post-4 Ma

Chapter 2: Background

Regional tectonic history

The evolution of the North American Cordillera can be traced back to the rifting of the Rodinia, but its major forming period was from mid Mesozoic to early Cenozoic. In this period, it was an accretionary arc-trench system, marked by the subduction of oceanic plates under the North American plate (Dickinson, 2004; Saleeby, 1983; Yonkee and Weil, 2015). The major features of the Cordilleran orogenic system, including the forearc accretionary prism and basin, the magmatic arc, the hinterland, the Sevier and Laramide fold-thrust belts, and the foreland basin, formed during this time (Yonkee and Weil, 2015). The decrease of the subduction dip from high angle to sub-horizontal during the subduction of the Farallon plate during late Cretaceous marks a major transition in the tectonic and magmatic pattern (Dickinson, 2004; Yonkee and Weil, 2015). From ~53-48 Ma, the Siletzia terrain was accreted to the North American Plate (Eddy et al., 2017). Following the accretion, the subduction boundary jumped from near the craton margin to west of the accreted Siletzia terrain (Eddy et al., 2017).

Large batholiths are widely distributed across the Cordillera, including in Idaho (DeCelles et al., 2009). The major batholith in Idaho, the Idaho batholith, occupies ~ 40000 km² and formed from 98 Ma to 54 Ma when pulses of magma were emplaced into the Precambrian basement crust. Initial low volume magmatism was metaluminous followed by high volume peraluminous magmatism (Gaschnig et al., 2010). Geochemistry shows that the metaluminous magmatism was mixed-source derived from crust and mantle, and the peraluminous magmatism was from the melting of crustal sources (Gaschnig et al., 2011). The Atlanta lobe of the batholith, where our study is located, is a peraluminous suite that was emplaced between 80 and 67 Ma. (Gaschnig et al., 2010).

Shortly after the placement of the Idaho batholith, the Cordilleran tectonic system transitioned from compressional to extensional, and in addition caused surface uplift, increased erosion and deposition rates, and magmatism, associated with thermodynamic effect and/or delamination (Humphreys, 1995; DeCelles et al., 2009; Cassel et al., 2018). There are three possible causes for this transition: (1). the movement pattern of the Farallon Plate turning from sub-horizontal subduction to slab rollback, (2). opening of a slab window due to the slab rollback (Humphreys, 1995) or ridge subduction (Breitsprecher et al., 2003; Duke 2009), and (3). slowing of the

convergence rate at the western plate boundary of the North American Plate (Constenius, 1996). The Challis magmatic event is potentially the result of these processes in Idaho lasting from 51 Ma to 43 Ma (Gaschnig et al., 2010). The Challis magmatism contains both volcanic and plutonic suites. The Challis volcanism is composed of intermediate to mafic lava flows along with tuff breccias in the early stage, and explosive eruptions with silicic flows and tuffs in the late stage (Moye et al., 1988; Sanford and Snee, 2005). The Challis dikes and plutons that cut into the batholith can be divided into a quartz diorite/monzodiorite suite and a pink/alkali-feldspar granite suite (Anderson, 1952; Ross, 1982). Due to the temporal and spatial similarities, the quartz monzodiorite suite is proposed to be linked to the earlier Challis volcanic events, and the pink granite suite to the later events (Lewis and Kiilsgaard 1991, McKervey 1998). Multiple metamorphic core complexes formed contemporaneously with the Challis magmatism, including the Bitterroot core complex in the northeastern Idaho batholith (Foster and Fanning, 1997; Foster et al., 2001; Foster and Raza, 2002) and the Pioneer core complex just east of the batholith (Vogl et al., 2012).

Multiple tectonic features (Figure 1) that could be associated with regional exhumation in the Cordillera started to form during the Miocene. In the early Miocene, Basin and Range extension was triggered by the formation of the San Andreas transform boundary and started to affect central Idaho at ~17 Ma (Dickinson, 2004; Janecke, 1992; Yonkee and Weil, 2015). Meanwhile, the CRB erupted from 17 Ma to 6 Ma in Washington, Idaho, and Oregon, forming a large igneous province (Hooper & Camp, 1981; Reidel et al., 2013). The majority (95% of the total volume) of the basalt erupted from 16.7 Ma to 15.9 Ma (Kasbohm & Schoene 2018). Traditional models consider a plume head or ponding of a plume under the slab that led to the eruption (Dodson et al., 1997; Camp & Ross, 2004; Hooper et al., 2007). Another model correlates the cause of the volcanism to the delamination of dense plutonic root resulting from the upwelling hot asthenosphere into space created by crustal extension, which has also been advocated to have caused regional uplift in the Wallowa Mountains (Hales et al., 2005; Hooper, 2007). The Yellowstone hotspot initiated at ~12 Ma, and since then propagated northeast towards the modern Yellowstone caldera, leaving silicic volcanic fields in its track (Pierce and Morgan, 1992). The track is along the topographically low Eastern Snake River Basin surrounded by Yellowstone crescent of high terrane. Both topographic features are suggested to be the result from the migration of the hotspot (Pierce and Morgan, 1992; Suppe et al., 1975).

The most widely accepted explanation for the hotspot track is having a stationary mantle plume beneath the moving North American Plate (Pierce and Morgan, 1992; Smith, 1978; Waschbusch and McNutt, 1994). Another idea is that the hotspot track is a series of delamination events that triggered each other or were triggered by a shared back-arc activity (Hales et al., 2005).

Geology of the study area

The Boise Mountains are located at the central-southern end of the Idaho batholith within the Atlanta lobe (Figure 1). The granodiorite and two-mica granite from the Idaho batholith here were intruded by the granite, granodiorite, and quartz monzodiorite from the Challis plutonic suites (Lewis et al., 2012). The faults in the area are mostly NW-SE trending normal faults. The displacement on the majority of the faults is poorly constrained, but some fault blocks have > 2km exhumation since 11 Ma (Vogl et al., 2014).

Previous studies indicated that the paleo topography of southern Idaho, including the study region, was a crustal plateau at least from the placement of the Atlanta lobe in the Cretaceous through the Eocene, and possibly into the Oligocene, as the plateau eroded to a low-relief landscape (e.g., Heller et al., 1985; Wolfe et al., 1998; Kent-Corson et al., 2006; Chetel et al., 2011; Gaschnig et al., 2011; Dumitru et al., 2013; Byerly et al., 2017; Dumitru et al., 2016; Fayon et al., 2017; Wetzell and Stanley, 2022). The modern topography of the region is composed of low relief mountain tops cut by deeply incised canyons, or sometimes referred to as an “elevated peneplain”. This topography is suggested to be a dissected plateau, where the flat mountain tops are the relict erosional surface from the low-relief paleo crustal plateau (Lindgren, 1904; Blackwelder, 1912; Umpleby, 1912; Larimer et al., 2018;). The timing of the dissection is suggested to be either late Miocene to Pliocene (Larimer et al., 2018; Blackwelder, 1912), or Eocene (Umpleby, 1912). To the west of the study region, paleo-Lake Idaho was located in the WSRP from 9.5 Ma to 1.7 Ma. The lake level reached its highest level of ~1160 m elevation, from ~ 6-4 Ma, and spilled over into the paleo Hells Canyon near Weiser, Idaho. The draining started no later than 4 Ma with the lake level dropping at the rate of 120 m/Ma and the base level drop continued in the same rate after the lake basin was filled with sediments as the downcutting of the outlet continued (Wood and Clemens, 2002). The drainage of the lake and the following base level drop has been considered as the cause of recent plateau

dissection conventionally (Meyer & Leidecker, 1999). However, recent works argued that instead of solely base level drop due to the lake draining, geodynamic rock uplift in central Idaho or a combination of both factors are more likely to be the driver of the incision (Larimer et al., 2018; Zhou and Liu, 2019).

Previous cooling and exhumation study in the Atlanta lobe

Multiple thermochronology, geochronology, and geomorphology methods have been applied to the Atlanta lobe to study the cooling, uplift, and incision history, including biotite $^{40}\text{Ar}/^{39}\text{Ar}$ (closure temperature T_c : ~400-350 °C), biotite K-Ar (T_c : ~300-200 °C), zircon fission track (T_c : ~250-175 °C) and apatite fission track (T_c : ~120-75 °C), zircon (U-Th)/He (T_c : ~210-25 °C), apatite (U-Th)/He (T_c : ~120-30°C), river incision and channel profile analyses (Dodson, 1973; Turner and Forbes, 1976; Criss et al., 1982; Sweetkind and Blackwell, 1989; Grove and Harrison, 1996; Vogl et al., 2014; Byerly et al., 2017; Fayon et al., 2017; Larimer et al., 2018; Ault et al., 2019; Mitchell & Yanites, 2019; Wetzel and Stanley, 2022). However, the application of the apatite (U-Th)/He dating in the Atlanta lobe was very limited, especially in the Boise Mountains (a total of 10 samples from Vogl et al. (2014) and Wetzel and Stanley (2022)) (Figure 1).

From previous works, the interior of the Atlanta lobe seems to have a different cooling history compared to its rim. Criss et al. (1982), Sweetkinnd and Blackwell (1989), and Fayon et al. (2017)'s works indicate that the western and eastern margin of the Atlanta lobe has an older cooling age (95 Ma for K-Ar, >40 Ma for apatite fission track, up to 82.5 Ma for zircon fission track, and 57 Ma for zircon (U-Th)/He), and the center has a younger cooling age (37 Ma for K-Ar, <35 Ma for apatite fission track, ~ 38 Ma for zircon fission track, and 20 Ma for zircon (U-Th)/He). Wetzel and Stanley (2022) have similar observations in the Boise Mountains. Their Bogus Basin transect at the western rim of the Boise Mountains, next to the WSRP basin-bounding Boise Front fault system at its footwall block, yields Eocene AHe dates only, while their Challis transect at the interior of the Boise Mountains yields exclusively Miocene AHe dates.

Combining the previous work, it seems there is a major Eocene cooling period across the Idaho batholith, followed by a late Miocene rapid cooling period for southern Atlanta lobe. For Eocene, during and after the Challis Magmatism, a period of rapid exhumation was

suggested by Wetzel and Stanley (2022) based on the Eocene cooling dates for AHe, AFT, ZHe, and ZFT samples from Sweetkind and Blackwell (1989), Fayon et al. (2017), and Wetzel and Stanley (2022). The exhumation might be followed by a topographic relief reduction based on the negative date-elevation trend Wetzel and Stanley (2022) observed in the Owyhee Mountains. For late Miocene, it seems the rapid cooling is mainly associated with the southern Atlanta lobe. Sweetkind and Blackwell (1989) suggested rapid exhumation < 10 Ma to a maximum of 3 km at river valley bottom of southern Atlanta lobe. Wetzel and Stanley (2022) speculated landscape rejuvenation and incision < 18 Ma based on limited Miocene AHe dates observed only in the Boise Mountains. Larimer et al. (2018) and Mitchell and Yanites (2019) suggested high incision rate across the exposed Atlanta lobe from 13-8 Ma to present likely due to a northward landscape tilting event originating from southern Atlanta lobe. The mechanism for the late Miocene cooling is still uncertain. Both Yellowstone-plume-caused rock uplift (Larimer et al., 2019; Mitchell & Yanites, 2019; Wetzel and Stanley, 2022) and base-level drop due to the subsidence of WSRP (Wetzel and Stanley, 2022) or the drainage of the paleo-Lake Idaho (Sweetkind and Blackwell, 1989; Larimer et al., 2019; Mitchell & Yanites, 2019; Wetzel and Stanley, 2022) have been invoked to explain this rapid rejuvenation. Although not located in the Atlanta lobe, the Pioneer Mountains to the east has AHe data that also suggests a late Miocene rapid rejuvenation from 11-8 Ma resulting in a >2-3 km exhumation (Vogl et al., 2014).

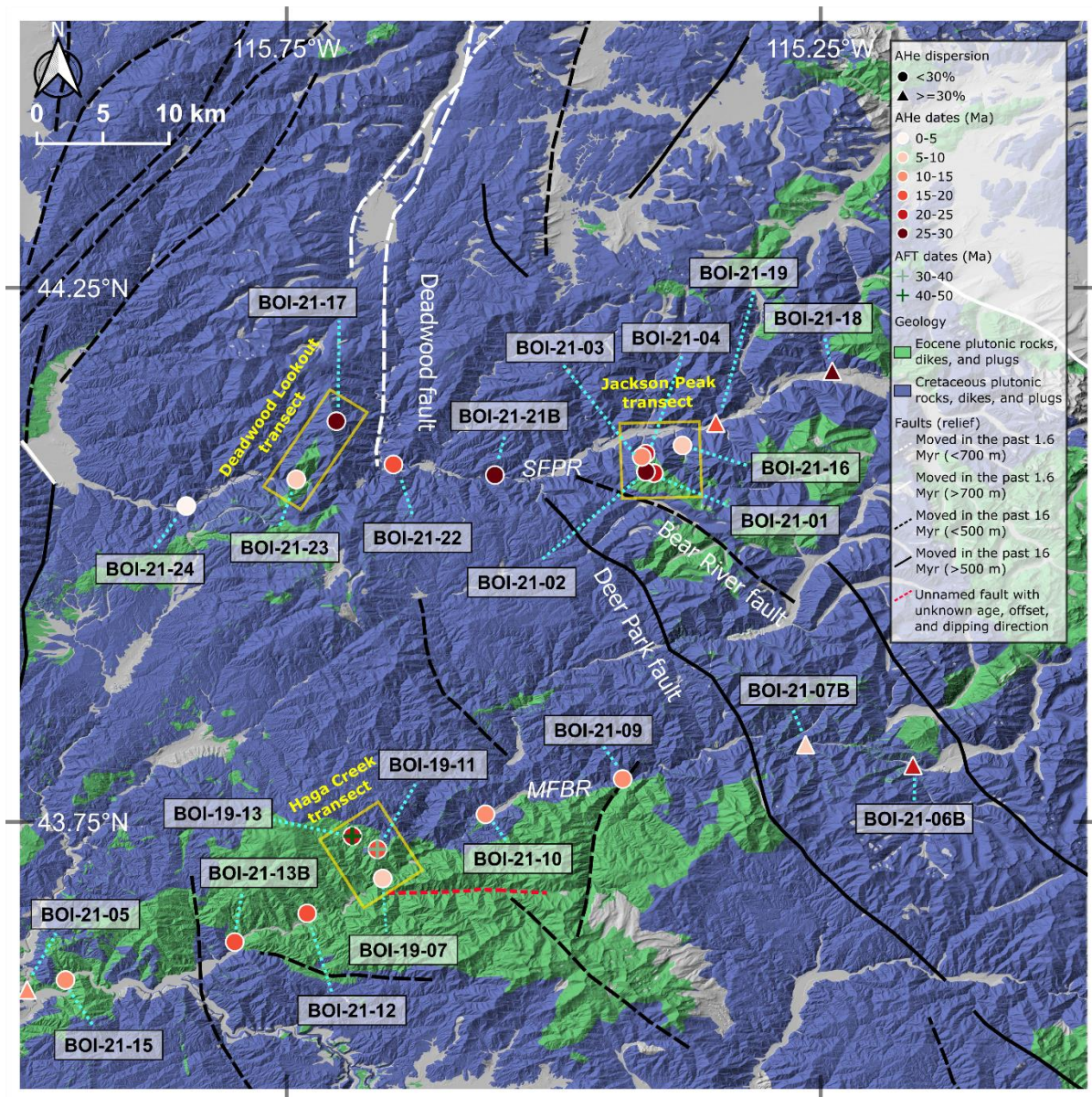


Figure 2. Geologic map of the Boise Mountains. Apatite (U-Th)/He (AHe) and fission track (AFT) samples from this study are highlighted with color indicating cooling dates. The location of faults younger than 16 Ma are reported with their offset range. Deadwood fault, Bear River fault, and Deer Park fault shown in Figure 5 are labeled. The yellow boxes label the 3 vertical transects for inverse modeling. Geologic map modified from Kiilgaard et al. (2001) and Kiilgaard et al. (2006). Fault data modified from Breckenridge et al. (2003) and Kiilgaard et al. (2001).

Chapter 3: Methods

Sampling strategy

Three vertical and two horizontal transects were sampled along the MFBR and the SFPR in the Boise Mountains (Figure. 2). The vertical transects were composed of samples that were within a short horizontal distance but had a large span of elevation, mostly collected along steep mountain slopes. The vertical transects were collected because if we assume that the samples moved as with a crustal block, the correlation between the samples from different elevations along the vertical transects would yield more information (Braun, 2002). These vertical transects were used for jointed inverse thermal history modeling to constrain the timing of regional exhumation. The first vertical transect was sampled at Jackson Peak, located toward the upstream end of the SFPR. It contains 5 samples that have elevation gaps of ~200 vertical m in between, with a total elevation range of 1000 m. The second vertical transect was sampled by Wetzel and Stanley (2022). It is the Haga Creek transect (previously termed the Challis transect in Wetzel and Stanley, 2022) in the MFBR and contains 3 samples. The third transect is the Deadwood transect located downstream SFPR, formed by 1 sample at mountain top and 1 sample at river level. All the samples from the vertical transects are Challis plutons/dikes. The horizontal transects were sampled along the two rivers at the river surface elevation. They were used to investigate the river incision history and potential spatial variation of the exhumation. The horizontal transects contain 11 samples for the MFBR and 8 samples for the SFPR. Because a portion of the samples did not yield enough high-quality apatite grains, we ended up getting 9 samples and 7 samples dated for the MFBR and the SFPR transects accordingly. Samples in the horizontal transects are ~8 km away from each other and cover the majority of the river. The MFBR transect and the SFPR transect are about 101 km and 71 km long, respectively. Cretaceous Atlanta lobe of the Idaho batholith, Eocene Challis plutonic igneous rocks, and Eocene Challis dikes that are likely to bear apatite minerals were collected, mostly granite and granodiorite. Whenever possible, Eocene rocks were picked over the Cretaceous rocks in order to focus on the more recent cooling history. Weathered rocks were avoided to reduce the chance of getting apatite grains with rough or stained surfaces.

Apatite (U-Th)/He dating

We acquired the apatite grains from collected samples by crushing, milling, sieving below 500

μm , separating denser minerals using water and lithium metatungstate, and separating non-magnetic mineral using a hand magnet and a Frantz magnetic separator. Individual aliquots of apatite grains were picked using a Leica binocular microscope paired with a digital camera under reflected, transmitted, and polarized light. Grains with little mineral and liquid inclusions, low surface roughness, euhedral crystal form, little surface staining, and width larger than 60 μm were selected. Picked grains were measured to obtain grain dimensions, sealed into individual Nb packets under the microscope using tweezers, and sent to the University of Colorado Boulder TRaIL for (U-Th)/He dating. At TRaIL, the Nb packets were heated with a laser to degas and collect radiogenic ^4He . The extracted ^4He was spiked and cleaned. A Balzers PrismaPlus QME 2200 quadrupole mass spectrometer was then used to analyze the ^4He . After degassing, the apatite grain packed in the Nb tube was spiked with tracer, heated, and dissolved in HNO_3 . The sample solution was then analyzed for the radioactive U, Th, Sm parent content with either a Thermo Element 2 magnetic sector ICP-MS or an Agilent 7900 quadrupole ICP-MS. The He dates of the aliquots were then calculated using methods from Ketcham et al. (2011).

Each sample consists of 7 to 4 individual apatite grains other than sample BOI-21-08B (Table 2). The two-sided Grubbs' test (Grubbs, 1950) was applied to each sample to look for outliers at significance level of 0.005. The outliers are shown in italics in Table 2 but not used for the later analysis or the calculation of mean and standard deviation. The mean and standard deviation for each sample were calculated (Table 2). The coefficient of variation (dispersion) of each sample was then calculated by dividing the sample standard deviation by the mean. The apatite He date of the samples with coefficient of variation <0.3 were reported as the mean of the individual grain dates and considered representative of a single population. The standard deviation of the date was used as the error range. The rest of the samples were considered to have dispersed grain dates and we did not report the sample mean or include them in thermal/landscape evolution analysis.

Thermal history modeling

Inverse modeling using both HeFTy ver. 2.1.4 (Ketcham, 2005) and QTQt ver. 20210903 (Gallagher, 2012) software was applied to jointly model the samples in each vertical transect to investigate the cooling histories compatible with the data. The reason we used multi-sample

joint modeling is that it allows samples to have their temperature and depth/elevation to be correlated to each other during inverse modeling, which makes the derived thermal history better constrained and represent the regional block exhumation status. Transects modeled include the Jackson Peak vertical transect with AHe dates, the Haga Creek vertical transect with previously published AHe dates (Wetzel & Stanley, 2022) and new AFT dates, and the Deadwood Lookout transect with AHe dates. For the HeFTy modeling, RDAAM He kinetic model was used (Flowers et al., 2009). Samples' mean values were used for the HeFTy, including mean value of uncorrected AHe dates, equivalent-FT-sphere radius, U, Th, and Sm concentration, and standard deviation of the uncorrected dates (if >10% of mean) as 1σ error (Table 3). If the standard deviation was <10% of mean, then 10% of mean was used as uncertainty. For our vertical transect samples, only sample BOI-21-17 has standard deviation <10% of the mean. The HeFTy multi-sample modeling function was run under t-Z mode, with the highest samples of each transect set as controlling samples that controlled the depth of the lower samples. For QTQt models, we input the individual grain uncorrected AHe dates, and 1σ analytical uncertainty of uncorrected dates as 1σ error (Table 3). We also input AFT data and modeled it together with the AHe data for QTQt models of the Haga Creek transect. The major geological constraint applied is the emplacement time range and initial temperature range. The date range of the emplacement of the sampled vertical transect rocks was set to be 52–42 Ma for the Eocene Challis rocks (Gaschnig et al., 2010). The initial temperature range was set to be 200-120 °C. More detailed model input and parameters are reported in Table 3.

We utilized both inverse modeling software to combine their strengths and complement their weaknesses. HeFTy uses a Frequentist algorithm with built-in “quality-control” statistical hypothesis tests that assess the model fit and reject inappropriate thermal history models generated from bad data (Vermeesch and Tian, 2014). However, this quality-control mechanism from the Frequentist algorithm can sometimes become too strict when dataset is precise (small error) or large (especially for multi-sample modeling) (Vermeesch and Tian, 2014). Due to this reason, we had to use sample mean for our HeFTy models, because if we used eU bins or individual grain data, the HeFTy simulation would not yield any acceptable models. The use of mean sample value, however, could potentially reduce the accuracy of the models. Even with the sample mean value approach, our Haga Creek transect still did not yield good-fit HeFTy models and our Deadwood Lookout transect did not yield any acceptable

HeFTy models. On the other hand, QTQt uses a Bayesian Markov Chain Monte Carlo (MCMC) algorithm that compares the relative likelihood between a randomly generated new model and the previous old model to accept or reject new models and look for “best-fit” models (Vermeesch and Tian, 2014). The early models generated in the “burn-in” period will be discarded and not plotted. After enough (number set by users) iterations of models are done in the “burn-in” period, QTQt enters the “post-burn-in” period and starts plotting newly accepted models (Gaschnig et al., 2010). The advantage of the MCMC algorithm is that it allows us to have a big and precise dataset using individual grain dates and analytical errors for our multi-sample modeling. Another advantage of QTQt is that while HeFTy uses fixed geothermal gradient through time, QTQt allows geothermal gradient to vary in a range through time as exhumation goes. The downside is that it might generate unrealistic thermal histories influenced by bad individual grain data in the data set, as it only compares the relative likelihood between models without statistical model fit control (Vermeesch and Tian, 2014). We expected that by comparing and combining HeFTy and QTQt inverse modeling results, we would have accurate thermal history inverse models for all our transects.

Table 2. Apatite (U-Th)/He Data

Sample Name and Aliquot [a]	length 1 (μm) [b]	width 1 (μm) [b]	length 2 (μm) [b]	width 2 (μm) [b]	Mass (μg) [c]	Rs (μm) [d]	Np[e]	⁴ He (nmol/g) [f]	U (ng) [g]	Th (ng) [h]	¹⁴⁷ Sm (ng) [i]	eU (ppm) [j]	eU Unc. (ppm) [k]	Uncorr Date (Ma) [l]	Uncorr Date Analytic (Ma) [m]	Combined Ft [n]	Corrected Date (Ma) [o]	Corr Date Analytic Unc. (Ma)2s [p]	
<u>Jackson Peak</u>																			
BOI-21-01: Tqmd (Eocene quartz monzodiorite suite): 44.0764°, -115.4061°, 2333 m elevation																			
a1	119.6	70.2	132.3	60.2	0.96	35.67	1T	1.84	0.0179	0.0686	0.0309	36.1	5.4	9.5	0.3	0.59	16.1	1.0	
a2	173.5	71.6	174.3	67.7	1.42	40.55	2T	0.99	0.0123	0.0450	0.0327	16.4	2.5	11.2	0.4	0.64	17.6	1.4	
a3	209.2	56.0	206.8	59.1	1.47	36.55	1T	0.86	0.0089	0.0336	0.0229	11.6	1.7	13.7	0.4	0.60	22.7	1.2	
a4	129.0	89.7	135.4	83.4	1.75	45.54	1T	2.26	0.0276	0.0683	0.0363	25.2	3.8	16.7	0.5	0.68	24.5	1.6	
Mean: 20.2 ± 3.5 Ma, 17% dispersion																			
BOI-21-02: Tqmd: 44.0777°, -115.4135°, 2470 m elevation																			
a1	255.9	101.1	251.2	92.6	4.60	56.64	1T	8.34	0.2533	0.1315	0.0842	62.0	9.3	24.9	0.5	0.75	33.3	1.3	
a2	188.8	58.9	187.4	60.2	1.24	36.75	2T	1.92	0.0162	0.0639	0.0403	25.7	3.9	13.8	0.4	0.60	23.0	1.3	
a3	130.9	72.9	114.1	71.6	1.19	39.99	1T	4.80	0.0499	0.0276	0.0251	47.8	7.2	18.6	0.5	0.65	28.7	1.5	
a5	252.6	62.6	252.8	62.2	1.90	39.38	2T	1.19	0.0140	0.0473	0.0493	13.5	2.0	16.3	0.5	0.63	25.9	1.5	
Mean: 27.7 ± 3.8 Ma, 14% dispersion																			
BOI-21-03: Tqmd: 44.0916°, -115.4174°, 2050 m elevation																			
a1	226.7	94.7	226.4	88.6	3.18	52.84	2T	1.09	0.0385	0.1481	0.1041	23.4	3.5	8.6	0.2	0.72	12.0	0.5	
a2	295.3	104.4	289.9	98.7	5.29	60.15	2T	2.02	0.0862	0.2948	0.1304	29.7	4.5	12.6	0.2	0.75	16.8	0.5	
a3	189.0	66.1	190.1	66.0	1.48	39.96	2T	1.47	0.0236	0.0918	0.0510	30.9	4.6	8.8	0.2	0.63	14.0	0.6	
a4	192.2	90.7	185.3	79.9	2.15	47.24	2T	1.28	0.0238	0.0978	0.0599	22.1	3.3	10.7	0.2	0.68	15.6	0.5	
a5	157.5	76.8	157.5	73.9	1.42	42.37	2T	1.21	0.0259	0.0883	0.0555	33.3	5.0	6.7	0.2	0.65	10.3	0.6	
Mean: 13.7 ± 2.3 Ma, 17% dispersion																			
BOI-21-04: Tqmd: 44.0946°, -115.4138°, 1775 m elevation																			
a1	126.4	87.9	121.6	86.2	1.67	45.51	1T	2.11	0.0393	0.0683	0.0557	33.5	5.0	11.7	0.2	0.68	17.1	0.7	
a2	161.3	134.9	164.5	132.0	3.29	59.64	2T	3.48	0.1101	0.1780	0.1607	46.7	7.0	13.8	0.2	0.75	18.3	0.6	
a3	188.2	120.2	182.2	130.4	6.82	68.47	0T	2.60	0.1572	0.2821	0.1787	33.1	5.0	14.6	0.2	0.79	18.5	0.6	
a4	230.4	128.3	226.5	132.6	7.40	71.94	1T	1.48	0.0826	0.1224	0.1342	15.2	2.3	18.0	0.2	0.80	22.6	0.6	
a5	215.6	124.1	215.6	103.4	3.97	59.42	2T	3.74	0.1059	0.1796	0.1568	37.7	5.7	18.4	0.3	0.75	24.4	0.8	
Mean: 20.2 ± 2.8 Ma, 14% dispersion																			
BOI-21-16: Tqmd: 44.1023°, -115.3793°, 1404 m elevation																			
a1	163.4	111.3	164.8	102.8	2.51	53.40	2T	0.62	0.0088	0.0614	0.0539	9.5	1.4	12.2	0.5	0.71	16.9	1.4	
a3	167.3	137.6	175.3	141.8	5.79	68.76	1T	0.52	0.0451	0.1075	0.1281	12.4	1.9	7.7	0.3	0.78	9.8	0.9	
a4	143.9	144.8	138.6	138.2	4.40	62.90	1T	0.22	0.0259	0.0469	0.0861	8.6	1.3	4.8	0.1	0.77	6.2	0.4	
a5	97.7	66.1	96.6	68.4	0.80	35.87	1T	0.39	0.0041	0.0210	0.0207	11.6	1.7	6.3	0.3	0.59	10.6	1.0	
Mean: 8.9 ± 1.9 Ma, 22% dispersion																			

(continued)

Table 2. Apatite (U-Th)/He Data (*continued*)

Sample Name and Aliquot [a]	length 1 (μm) [b]	width 1 (μm) [b]	length 2 (μm) [b]	width 2 (μm) [b]	Mass (μg) [c]	Rs (μm) [d]	Np[e]	⁴ He (nmol/g) [f]	U (ng) [g]	Th (ng) [h]	¹⁴⁷ Sm (ng) [i]	eU (ppm) [j]	eU Unc. (ppm) [k]	Uncorr Date (Ma) [l]	Uncorr Date Analytic Unc. (Ma) [m]	Combined Ft [n]	Corrected Date (Ma) [o]	Corr Date Analytic Unc. (Ma)2s [p]
<u>Middle Fork Boise River</u>																		
BOI-21-05: Tgd (Eocene granodiorite): 43.5925°, -115.9931°, 956 m elevation																		
a1	126.0	107.3	131.1	87.8	2.51	49.04	0T	1.28	0.0598	0.0476	0.1063	28.7	4.3	8.3	0.2	0.71	11.7	0.5
a2	265.5	93.8	266.1	100.7	4.56	59.12	2T	3.48	0.2391	0.2645	0.2557	66.7	10.0	9.7	0.3	0.75	12.8	0.8
a3	151.7	96.8	170.3	97.8	3.48	54.35	0T	2.07	0.1113	0.1511	0.1607	42.7	6.4	9.0	0.2	0.73	12.3	0.6
a4	172.0	86.0	171.0	76.1	1.73	44.79	2T	7.43	0.0847	0.0953	0.1007	62.4	9.4	22.1	0.4	0.68	32.4	1.3
a5	141.2	76.1	143.1	72.2	1.47	41.70	1T	9.28	0.0451	0.0847	0.0708	44.9	6.7	38.3	0.7	0.65	58.4	2.2
a01	182.0	89.4	184.9	83.2	2.16	48.07	2T	114.32	0.1140	0.1150	0.1560	66.0	9.9	7.2	0.1	0.70	10.2	0.1
a02	117.1	85.7	116.3	69.1	0.86	37.30	2T	21.91	0.0110	0.0090	0.0440	14.9	2.2	6.0	0.3	0.62	9.5	0.5
54% dispersion of AHe dates																		
BOI-21-06B: Kbgd (Cretaceous biotite granodiorite): 43.8028°, -115.1634°, 1576 m elevation																		
a1	157.3	76.2	155.6	76.0	1.45	43.11	2T	1.95	0.0349	0.0528	0.0942	33.2	5.0	10.9	0.3	0.66	16.3	0.9
a2	173.4	75.0	175.4	76.1	1.68	44.20	2T	4.76	0.0538	0.0549	0.0943	40.3	6.0	21.9	0.7	0.68	32.3	2.1
a3	185.1	105.6	185.3	109.7	3.20	57.83	2T	1.97	0.0522	0.0802	0.1172	22.6	3.4	16.2	0.5	0.75	21.6	1.2
a4	194.5	93.8	198.4	87.6	3.07	51.70	1T	1.81	0.0728	0.1189	0.2239	33.5	5.0	10.0	0.2	0.72	13.9	0.6
a5	157.1	146.4	157.9	141.9	5.31	66.99	1T	3.11	0.1760	0.2749	0.3700	46.0	6.9	12.5	0.3	0.78	16.0	0.8
a01	136.1	88.6	136.1	82.7	1.37	43.74	2T	193.54	0.0260	0.0780	0.0920	33.1	5.0	24.0	0.6	0.66	35.9	0.9
a02	134.1	85.8	138.3	89.8	1.47	46.13	2T	158.56	0.0170	0.0130	0.0700	13.5	2.0	47.5	2.7	0.69	68.4	3.9
37% dispersion of AHe dates																		
BOI-21-07B: Trd (Eocene rhyodacite dikes): 43.8222°, -115.264°, 1463 m elevation																		
a1	143.1	84.9	145.1	85.9	1.54	45.54	2T	1.65	0.0331	0.0629	0.0928	31.8	4.8	9.6	0.4	0.68	14.1	1.2
a2	87.8	86.7	88.9	82.8	1.00	39.21	1T	0.16	0.0081	0.0146	0.0286	11.7	1.8	2.6	0.3	0.63	4.0	0.9
a3	142.8	115.2	143.5	115.7	2.22	52.38	2T	0.28	0.0118	0.0352	0.1016	9.5	1.4	5.6	0.3	0.72	7.7	0.7
a4	195.7	195.5	193.3	180.8	10.73	83.62	1T	0.69	0.0849	0.2170	0.4210	13.0	2.0	9.8	0.2	0.82	11.9	0.4
a5	106.4	69.9	105.5	66.0	1.09	37.61	0T	0.86	0.0191	0.0200	0.0428	22.2	3.3	7.2	0.2	0.62	11.4	0.7
36% dispersion of AHe dates																		
BOI-21-08B: Trd: 43.8187°, -115.3532°, 1348 m elevation																		
a1	166.4	138.9	170.3	133.9	5.30	66.37	1T	0.39	0.0320	0.1530	0.0881	13.0	2.0	5.5	0.1	0.77	7.1	0.4
Only one grain reported. Other grains have eU < 5 ppm thus are not reported																		

(continued)

Table 2. Apatite (U-Th)/He Data (*continued*)

Sample Name and Aliquot [a]	length 1 (μm) [b]	width 1 (μm) [b]	length 2 (μm) [b]	width 2 (μm) [b]	Mass (μg) [c]	Rs (μm) [d]	Np[e]	⁴ He (nmol/g) [f]	U (ng) [g]	Th (ng) [h]	¹⁴⁷ Sm (ng) [i]	eU (ppm) [j]	eU Unc. (ppm) [k]	Uncorr Date (Ma) [l]	Uncorr Date Analytic Unc. (Ma) [m]	Combined Ft [n]	Corrected Date (Ma) [o]	Analytic Unc. (Ma)2s [p]	Corr Date
<u>Middle Fork Boise River (<i>continued</i>)</u>																			
BOI-21-09: Tg (Eocene granite): 43.79°, -115.4353°, 1248 m elevation																			
a1	96.1	90.3	98.6	80.8	1.54	43.17	0T	1.93	0.0473	0.0065	0.0254	31.9	4.8	11.2	0.4	0.68	16.6	1.2	
a2	153.0	87.6	151.2	88.1	2.21	48.75	1T	7.45	0.0460	0.0361	0.0443	24.9	3.7	55.3	1.7	0.71	78.0	4.8	
a3	107.4	76.3	106.7	66.0	0.69	35.05	2T	0.19	0.0032	0.0058	0.0073	6.6	1.0	5.2	0.7	0.59	8.7	2.5	
a4	114.2	66.0	114.3	71.0	0.79	37.07	2T	0.94	0.0154	0.0028	0.0136	20.3	3.1	8.6	0.5	0.63	13.7	1.7	
a02	112.2	96.3	115.2	84.6	1.04	41.19	2T	24.84	0.0090	0.0120	0.0190	11.3	1.7	9.1	0.5	0.65	13.9	0.7	
Mean: 13.2 ± 2.8 Ma, 21% dispersion																			
BOI-21-10: Kbgd: 43.757°, -115.5638°, 1139 m elevation																			
a1	113.2	96.5	112.8	55.0	0.78	34.35	1T	0.61	0.0098	0.0027	0.0382	13.8	2.1	8.2	0.7	0.60	13.6	2.2	
a2	155.1	106.8	158.5	103.0	3.08	55.07	1T	2.18	0.0472	0.0705	0.1455	21.1	3.2	19.1	0.3	0.74	25.8	0.8	
a3	141.9	128.4	146.8	125.6	3.85	60.57	1T	0.44	0.0391	0.0196	0.1497	11.7	1.8	7.0	0.3	0.76	9.1	0.7	
a4	102.5	87.0	107.4	82.1	1.67	44.14	0T	1.34	0.0383	0.0229	0.0680	26.6	4.0	9.3	0.4	0.68	13.7	1.3	
a5	199.9	136.3	199.1	121.3	5.75	66.65	1T	0.79	0.0638	0.0283	0.1946	12.5	1.9	11.7	0.3	0.79	14.8	0.8	
a01	162.4	109.3	162.4	89.6	2.10	49.08	2T	28.35	0.0240	0.0120	0.0910	12.9	1.9	8.9	0.4	0.71	12.4	0.5	
a02	169.5	110.7	145.7	111.3	3.25	61.97	1T	27.03	0.0340	0.0130	0.1190	11.6	1.7	9.5	0.3	0.77	12.3	0.3	
Mean: 12.6 ± 1.8 Ma, 14% dispersion																			
BOI-21-12: Tg: 43.6642°, -115.7308°, 998 m elevation																			
a1	123.1	88.6	122.1	60.1	0.99	35.33	1T	1.00	0.0149	0.0235	0.0404	21.0	3.2	8.9	0.4	0.60	14.8	1.2	
a2	191.0	83.7	189.7	88.7	2.38	50.00	2T	0.56	0.0127	0.0428	0.1024	10.0	1.5	10.4	0.4	0.70	14.7	1.3	
a3	146.8	69.9	150.7	67.0	1.34	39.52	1T	1.49	0.0136	0.0456	0.0872	18.8	2.8	14.7	0.4	0.63	23.1	1.3	
a4	123.2	99.5	121.3	77.0	1.08	40.30	2T	0.89	0.0093	0.0279	0.0739	15.2	2.3	10.8	0.7	0.64	16.7	2.0	
a5	163.5	72.1	167.5	72.1	1.70	42.43	1T	1.90	0.0218	0.0591	0.0624	21.4	3.2	16.5	0.8	0.65	25.0	2.4	
Mean: 18.9 ± 4.4 Ma, 23% dispersion																			
BOI-21-13B: Tr (Eocene rhyolite and rhyolite porphyry dikes and plugs): 43.6374°, -115.7987°, 1004 m elevation																			
a1	114.2	68.0	112.3	65.0	0.72	35.17	2T	1.33	0.0060	0.0269	0.0582	17.8	2.7	13.8	0.7	0.58	23.4	2.5	
a2	120.2	95.6	119.1	77.8	1.05	40.10	2T	0.83	0.0076	0.0312	0.0706	14.9	2.2	10.4	0.7	0.63	16.2	2.2	
a3	182.7	83.0	188.9	84.7	2.58	48.91	1T	0.78	0.0151	0.0740	0.1295	13.0	2.0	11.1	0.3	0.69	15.8	0.9	
a4	156.6	118.2	158.9	101.9	4.04	56.73	0T	0.37	0.0153	0.0793	0.1362	8.7	1.3	7.9	0.2	0.73	10.7	0.7	
a5	130.9	90.6	127.0	90.6	2.41	48.94	0T	0.54	0.0062	0.0316	0.0889	6.0	0.9	16.8	0.7	0.69	23.9	2.0	
Mean: 18.0 ± 5.0 Ma, 28% dispersion																			

(*continued*)

Table 2. Apatite (U-Th)/He Data (*continued*)

Sample Name and Aliquot [a]	length 1 (μm) [b]	width 1 (μm) [b]	length 2 (μm) [b]	width 2 (μm) [b]	Mass (μg) [c]	Rs (μm) [d]	Np[e]	⁴ He (nmol/g) [f]	U (ng) [g]	Th (ng) [h]	¹⁴⁷ Sm (ng) [i]	eU (ppm) [j]	eU Unc. (ppm) [k]	Uncorr Date (Ma) [l]	Uncorr Date Analytic (Ma) [m]	Combined Ft [n]	Corrected Date (Ma) [o]	Analytic Unc. (Ma)2s [p]	Corr Date
<u>Middle Fork Boise River (<i>continued</i>)</u>																			
BOI-21-15: Tgd: 43.6018°, -115.9572°, 946 m elevation																			
a1	105.3	78.8	110.2	82.7	0.88	38.86	2T	2.51	0.0366	0.1019	0.0452	69.4	10.4	6.7	0.1	0.62	10.7	0.5	
a2	117.7	115.2	118.5	77.0	1.47	41.79	1T	2.54	0.0509	0.0764	0.0547	47.4	7.1	9.9	0.3	0.66	15.1	0.9	
a3	115.3	86.2	121.1	85.7	1.54	44.62	1T	1.76	0.0510	0.0579	0.0454	42.2	6.3	7.7	0.3	0.68	11.4	1.0	
a4	199.8	87.6	201.8	76.8	2.19	46.74	2T	1.12	0.0376	0.0213	0.0443	19.6	2.9	10.5	0.4	0.70	15.1	1.2	
a5	252.2	102.7	254.2	95.8	4.20	57.66	2T	1.82	0.1279	0.1538	0.0912	39.3	5.9	8.6	0.2	0.75	11.5	0.6	
Mean: 12.8 ± 1.9 Ma, 15% dispersion																			
<u>Deadwood Lookout</u>																			
BOI-21-17: Tr: 44.125°, -115.7034°, 2295 m elevation																			
a1	170.1	116.2	169.6	105.1	2.75	55.07	2T	1.86	0.0228	0.0799	0.1093	15.5	2.3	22.2	0.6	0.73	30.4	1.6	
a2	135.3	88.9	140.3	94.9	1.60	46.93	2T	2.89	0.0244	0.0763	0.0777	26.9	4.0	19.9	0.5	0.68	29.0	1.4	
a3	224.8	95.8	225.6	82.2	2.88	50.09	2T	4.16	0.0457	0.1891	0.1343	31.9	4.8	24.2	0.5	0.70	34.4	1.5	
a4	138.9	107.7	138.9	101.1	1.83	48.92	2T	3.13	0.0165	0.0714	0.0882	18.7	2.8	31.0	0.8	0.69	44.5	2.3	
a5	171.5	116.0	174.4	121.0	3.26	59.23	2T	3.95	0.0695	0.2251	0.1316	38.0	5.7	19.3	0.4	0.75	25.8	1.2	
Mean: 29.9 ± 3.1 Ma, 10% dispersion																			
BOI-21-23: Thbg (Eocene hornblende-biotite granite): 44.0705°, -115.741°, 1047 m elevation																			
a1	158.8	88.8	159.6	71.0	1.44	41.75	2T	0.59	0.0285	0.1112	0.0532	38.3	5.7	2.9	0.1	0.64	4.4	0.4	
a2	185.1	88.8	180.2	78.9	2.38	47.06	1T	0.74	0.0472	0.1871	0.0790	38.8	5.8	3.6	0.1	0.68	5.2	0.3	
a3	212.7	90.6	212.5	82.7	2.63	49.59	2T	0.58	0.0486	0.1844	0.0833	35.4	5.3	3.1	0.1	0.70	4.4	0.2	
a4	250.9	86.7	253.3	69.0	2.80	44.25	1T	0.49	0.0374	0.1420	0.0756	25.7	3.9	3.6	0.1	0.66	5.4	0.4	
a5	170.6	89.5	167.2	78.5	2.17	46.27	1T	0.78	0.0369	0.1519	0.0735	33.9	5.1	4.2	0.1	0.68	6.3	0.4	
Mean: 5.1 ± 0.7 Ma, 13% dispersion																			
<u>South Fork Payette River</u>																			
BOI-21-18: Kbgd: 44.172°, -115.239°, 1502 m elevation																			
a1	123.0	84.7	124.1	79.8	1.48	43.42	1T	1.52	0.0153	0.0165	0.0325	13.2	2.0	21.4	1.2	0.67	31.8	3.6	
a2	130.0	88.6	129.0	83.7	1.71	45.48	1T	3.65	0.0297	0.0267	0.0628	21.4	3.2	31.5	1.0	0.69	45.7	2.8	
a3	137.8	103.4	141.0	98.5	3.17	53.55	0T	0.74	0.0440	0.0629	0.0792	18.8	2.8	7.3	0.2	0.73	9.9	0.5	
a4	130.9	107.4	132.9	93.6	2.19	49.52	1T	10.18	0.1976	0.2319	0.1654	116.0	17.4	16.3	0.3	0.71	23.0	0.8	
a5	168.3	143.8	165.7	130.1	3.45	60.37	2T	0.69	0.0332	0.0363	0.1201	12.4	1.9	10.3	0.3	0.76	13.5	0.8	
a01	130.9	99.5	131.9	92.6	1.50	46.35	2T	48.38	0.0170	0.0150	0.0460	13.8	2.1	14.4	0.3	0.69	20.8	0.4	
a02	107.5	86.0	106.3	79.1	0.86	38.93	2T	91.33	0.0090	0.0130	0.0300	14.2	2.1	26.3	1.0	0.63	41.6	1.6	
47% dispersion of AHe dates																			

(*continued*)

Table 2. Apatite (U-Th)/He Data (*continued*)

Sample Name and Aliquot [a]	length 1 (μm) [b]	width 1 (μm) [b]	length 2 (μm) [b]	width 2 (μm) [b]	Mass (μg) [c]	Rs (μm) [d]	Np[e]	⁴ He (nmol/g) [f]	U (ng) [g]	Th (ng) [h]	¹⁴⁷ Sm (ng) [i]	eU (ppm) [j]	eU Unc. (ppm) [k]	Uncorr Date (Ma) [l]	Uncorr Date Analytic Unc. (Ma) [m]	Combined Ft [n]	Corrected Date (Ma) [o]	Corr Date Analytic Unc. (Ma)2s [p]
<u>South Fork Payette River (<i>continued</i>)</u>																		
BOI-21-19: Trd: 44.1232°, -115.348°, 1376 m elevation																		
a1	183.1	117.2	190.1	78.4	3.12	47.07	0T	0.18	0.0087	0.0434	0.0502	6.2	0.9	5.4	0.3	0.68	7.9	0.9
a2	131.8	112.9	128.9	93.6	2.20	49.19	1T	2.23	0.0262	0.1019	0.0807	23.3	3.5	17.8	0.3	0.70	25.4	0.9
a3	127.0	88.6	124.1	74.8	1.07	40.21	2T	0.63	0.0135	0.0302	0.0413	19.6	2.9	5.9	0.2	0.64	9.2	0.6
a4	142.8	90.7	142.8	85.7	2.01	47.19	1T	1.64	0.0219	0.1071	0.0628	23.9	3.6	12.8	0.3	0.68	18.7	0.8
a5	290.8	169.9	287.5	128.5	12.48	76.43	0T	2.56	0.2544	0.2451	0.1738	25.2	3.8	18.9	0.4	0.81	23.3	1.0
42% dispersion of AHe dates																		
BOI-21-21B: Tr: 44.0746°, -115.555°, 1211 m elevation																		
a1	172.6	85.3	174.3	81.2	1.90	46.80	2T	1.76	0.0155	0.0162	0.1220	10.7	1.6	30.5	1.2	0.69	43.3	3.5
a2	124.2	102.9	123.9	82.5	1.21	42.17	2T	7.03	0.0567	0.0917	0.0575	65.5	9.8	19.9	0.4	0.66	30.2	1.1
a3	120.1	65.0	122.1	67.0	1.01	37.62	1T	1.79	0.0139	0.0165	0.0592	18.1	2.7	18.4	0.8	0.62	29.2	2.5
a4	136.9	107.3	135.8	65.3	1.33	38.00	1T	2.04	0.0201	0.0492	0.1053	24.5	3.7	15.4	0.4	0.62	24.7	1.1
a5	174.2	83.7	173.3	78.0	1.80	45.58	2T	0.53	0.0091	0.0077	0.0794	6.4	1.0	15.2	1.2	0.69	21.7	3.5
a01	98.5	83.7	97.5	74.8	0.68	35.79	2T	89.65	0.0140	0.0190	0.0640	26.8	4.0	13.6	0.6	0.60	22.4	0.9
Mean: 25.6 ± 3.5 Ma, 14% dispersion																		
BOI-21-22: Kbgd: 44.0845°, -115.65°, 1150 m elevation																		
a1	119.1	94.5	126.0	94.5	1.91	48.08	1T	2.32	0.0268	0.0179	0.1057	16.7	2.5	25.7	1.2	0.70	36.2	3.4
a2	284.5	92.6	282.5	78.8	3.98	50.36	1T	0.49	0.0232	0.0244	0.1939	7.7	1.2	11.8	0.5	0.71	16.3	1.4
a3	189.1	131.0	181.2	105.4	3.26	57.40	2T	0.80	0.0255	0.0315	0.1956	10.6	1.6	13.9	0.4	0.75	18.5	1.0
a4	225.7	157.0	224.6	159.7	10.17	81.66	1T	0.57	0.0491	0.0797	0.3719	7.0	1.0	15.1	0.3	0.82	18.3	0.8
a5	289.6	185.3	289.2	142.8	12.78	82.29	1T	0.55	0.0716	0.0924	0.4219	7.6	1.1	13.5	0.2	0.82	16.4	0.5
Mean: 17.4 ± 1.0 Ma, 6% dispersion																		
BOI-21-24: Kbgd: 44.0456°, -115.844°, 1039 m elevation																		
a1	126.9	98.2	121.9	88.4	1.82	46.74	1T	0.07	0.0095	0.0116	0.0990	7.2	1.1	1.7	0.2	0.69	2.4	0.6
a2	154.7	138.0	154.6	117.2	3.98	60.16	1T	0.14	0.0220	0.0289	0.2235	7.7	1.2	3.3	0.2	0.76	4.3	0.4
a3	141.7	111.5	136.8	99.7	2.59	52.36	1T	0.11	0.0132	0.0174	0.1511	7.2	1.1	2.9	0.1	0.72	4.0	0.4
a4	109.3	135.8	108.5	91.9	2.49	48.24	0T	0.10	0.0136	0.0144	0.1433	7.3	1.1	2.5	0.2	0.70	3.5	0.4
a5	158.4	156.4	155.8	150.7	5.84	69.08	1T	0.13	0.0254	0.0303	0.2409	5.9	0.9	4.1	0.1	0.79	5.2	0.3
a01	102.4	95.6	102.4	89.6	1.41	43.83	1T	44.45	0.0180	0.0240	0.0960	17.1	2.6	10.6	0.4	0.67	15.6	0.6
a02	159.7	66.0	156.8	61.2	1.07	37.53	2T	5.20	0.0070	0.0070	0.0620	8.1	1.2	2.5	0.3	0.62	4.0	0.5
Mean: 3.9 ± 0.8 Ma, 21% dispersion																		

(*continued*)

Table 2. Apatite (U-Th)/He Data (continued)

Sample Name and Aliquot [a]	length 1 (μm) [b]	width 1 (μm) [b]	length 2 (μm) [b]	width 2 (μm) [b]	Mass (μg) [c]	Rs (μm) [d]	Np[e]	⁴ He (nmol/g) [f]	U (ng) [g]	Th (ng) [h]	¹⁴⁷ Sm (ng) [i]	eU (ppm) [j]	eU Unc. (ppm) [k]	Uncorr Date (Ma) [l]	Uncorr Date Analytic (Ma) [m]	Combined Ft [n]	Corrected Date (Ma) [o]	Corr Date Analytic Unc. (Ma)2s [p]
Haga Creek (Wetzel&Stanley, 2022)																		
BOI-19-07: Tei (Eocene Granite and quartz monzodiorite): 43.69686°, -115.66013°, 1058 m elevation																		
a1	119.3	71.0	123.5	69.2	0.88	36.35	2T	1.16	0.0283	0.0570	0.0668	47.6	7.1	4.4	0.2	0.61	7.3	0.6
a2	115.2	61.1	119.1	66.0	0.92	34.69	1T	0.28	0.0078	0.0087	0.0387	10.7	1.6	4.6	0.4	0.60	7.6	1.3
a3	120.0	64.4	122.4	62.2	0.92	34.14	1T	0.27	0.0069	0.0278	0.0517	14.7	2.2	3.3	0.2	0.57	5.6	0.6
a4	201.9	71.9	203.1	71.0	1.84	41.87	2T	0.82	0.0248	0.1176	0.1233	28.5	4.3	5.2	0.2	0.64	8.1	0.7
a5	129.0	67.0	128.4	65.8	1.08	36.06	1T	0.58	0.0092	0.0462	0.0611	18.6	2.8	5.7	0.3	0.59	9.4	0.9
a6	180.1	95.5	179.5	87.7	2.80	49.10	1T	0.71	0.0301	0.1111	0.1623	20.1	3.0	6.4	0.2	0.70	9.0	0.5
Mean: 7.9 ± 1.4 Ma, 17% dispersion																		
BOI-19-11: Tei: 43.72419°, -115.665°, 1423 m elevation																		
a1	139.2	83.9	140.0	76.9	1.64	41.83	1T	0.67	0.0171	0.0140	0.0797	12.5	1.9	9.7	0.6	0.67	14.3	1.8
a2	131.1	86.7	130.1	83.7	1.71	43.36	1T	0.51	0.0134	0.0094	0.0874	9.1	1.4	10.0	0.3	0.68	14.4	0.9
a3	161.7	129.2	157.7	134.0	4.78	62.50	1T	0.65	0.0278	0.0206	0.1914	6.8	1.0	16.7	0.7	0.78	21.4	2.0
a4	154.7	116.2	147.7	113.2	3.45	55.66	1T	1.01	0.0330	0.0237	0.1733	11.2	1.7	16.2	0.4	0.75	21.5	1.0
a5	162.5	87.6	168.8	86.8	1.95	46.75	2T	0.83	0.0184	0.0127	0.0790	11.0	1.7	13.6	0.5	0.70	19.2	1.4
Mean: 18.2 ± 3.6 Ma, 20% dispersion																		
BOI-19-13: Tei: 43.73656°, -115.68853°, 1729 m elevation																		
a1	126.2	82.8	133.1	77.9	1.51	41.26	1T	3.62	0.0415	0.1125	0.0800	45.0	6.7	14.7	0.3	0.65	22.5	0.9
a2	130.0	71.9	136.9	73.9	1.09	38.85	2T	2.62	0.0284	0.0699	0.0555	41.2	6.2	11.6	0.3	0.63	18.4	1.1
a3	161.1	85.0	155.1	83.0	1.71	44.76	2T	2.42	0.0293	0.0705	0.0556	26.9	4.0	16.4	0.4	0.67	24.3	1.1
a4	203.8	94.5	201.0	95.6	3.58	53.01	1T	1.55	0.0408	0.1088	0.0836	18.5	2.8	15.3	0.3	0.72	21.1	0.8
a5	205.1	99.6	203.2	99.6	3.24	54.63	2T	1.05	0.0289	0.0923	0.0851	15.6	2.3	12.2	0.3	0.73	16.7	0.8
Mean: 20.6 ± 3.1 Ma, 15% dispersion																		

(continued)

Table 2. Apatite (U-Th)/He Data (continued)

Note: Rows in italics indicate outlier grains that are not included in mean calculation or inverse modeling. This table is modified from the recommendations and approach in Flowers et al. (2022a). The notes below are cited from the CU TRaIL AHe data report form.

a - Samples with <30% dispersion have their corrected dates mean and 1σ standard deviation reported. Samples with >30% dispersion don't have their mean reported and are not included in further data analysis. Dispersion is calculated as the standard deviation divided by the mean of the sample.

b - Mass is the mass of the crystal. Determined from the measured grain dimensions, the volume assuming the reported grain geometry, and the volume equations and mineral densities in Ketcham et al. (2011).

c - Length is measured parallel to the c-axis and includes pyramidal terminations. It is measured twice on two perpendicular sides.

d - R_s is the radius of a sphere with an equivalent alpha-ejection correction as the grain, calculated using equation A6 in Cooperdock et al. (2019).

e - N_p denotes the number of pyramidal terminations of the grain.

f - Concentration of He computed from the mass and the absolute amount of the measured isotopes (where ^{147}Sm is 0.15 of the total Sm reported here). In some cases Sm may not be measured, for example in minerals like zircon with negligible Sm. n.m. indicates when Sm is not measured.

g - Total blank-corrected ng of ^{238}U and ^{235}U . Total ^{238}U is measured and ^{235}U is calculated assuming $^{235}\text{U} = ^{238}\text{U}/137.818$ after Hiess et al. (2012).

h - Total blank-corrected ng of ^{232}Th .

i - Total blank-corrected ng of ^{147}Sm . In some cases Sm may not be measured, for example in minerals like zircon with negligible Sm. n.m. indicates when Sm is not measured.

j - eU is effective uranium concentration. Calculated as $U + 0.238 * \text{Th} + 0.0012 * \text{Sm}$ after Appendix A of Cooperdock et al. (2019).

k - 15% error of eU reported

l - Uncorrected (U-Th)/He date is calculated iteratively using the ^4He production equation defined as equation 1 in Wolf et al. (1998) modified to include He produced from Sm decay and assuming secular equilibrium.

m - Uncertainty on the uncorrected (U-Th)/He date is reported at 1σ and includes the propagated total analytical uncertainties (TAU) on the U, Th, Sm and He measurements.

n - The combined alpha-ejection correction for the crystal calculated from the parent isotope-specific FT corrections, the proportion of U and Th contributing to ^4He production, and assuming homogeneous parent isotope distributions using equation A4 in Cooperdock et al., (2019). The parent isotope-specific alpha ejection-corrections were computed assuming the reported grain geometry in this table and the equations and alpha-stopping distances in Ketcham et al., (2011).

o - The corrected (U-Th)/He date is calculated iteratively using the absolute values of He, U, Th and Sm, the isotope specific FT corrections, and equation 34 in Ketcham et al. (2011) assuming secular equilibrium.

p - Uncertainty on the corrected (U-Th)/He date is reported at 2σ and includes the propagated total analytical uncertainties (TAU) on the U, Th, Sm and He measurements. Uncertainty propagation done using HeCalc (Martin et al., 2023).

Table 3. Thermal History Modeling Input Table

1. Thermochronologic data

Samples and data used in simulations

<u>Sample</u>	<u>Rock Type</u>	<u>HeFTy AHe data input</u>	<u>QTQt AHe data input</u>	<u>QTQt AFT data input</u>	<u>Emplacement age used in model</u>
<u>Jackson Peak</u>					
BOI-21-01	Tqmd (Eocene quartz monzodiorite suite)	mean of 4 grains	4 individual grains	no AFT data	51-43 Ma (Gaschnig et al., 2010); box range: 52–42 Ma
BOI-21-02	Tqmd	mean of 4 grains	4 individual grains	no AFT data	51-43 Ma (Gaschnig et al., 2010); box range: 52–42 Ma
BOI-21-03	Tqmd	mean of 5 grains	5 individual grains	no AFT data	51-43 Ma (Gaschnig et al., 2010); box range: 52–42 Ma
BOI-21-04	Tqmd	mean of 5 grains	5 individual grains	no AFT data	51-43 Ma (Gaschnig et al., 2010); box range: 52–42 Ma
BOI-21-16	Tqmd	mean of 3 grains	3 individual grains	no AFT data	51-43 Ma (Gaschnig et al., 2010); box range: 52–42 Ma
<u>Deadwood Lookout</u>					
BOI-21-17	Tr (Eocene rhyolite and rhyolite porphyry dikes and plugs)	no HeFTy model	4 individual grains	no AFT data	51-43 Ma (Gaschnig et al., 2010); box range: 52–42 Ma
BOI-21-23	Thbg (Eocene hornblende-biotite granite)	no HeFTy model	5 individual grains	no AFT data	51-43 Ma (Gaschnig et al., 2010); box range: 52–42 Ma
<u>Haga Creek</u>					
BOI-19-07	Tgd (Eocene granodiorite)	mean of 6 grains	6 individual grains	no AFT data	48 ± 3 Ma (Gaschnig et al., 2010); box range: 52–42 Ma
BOI-19-11	Tgd	mean of 5 grains	5 individual grains	all 40 spots	48 ± 3 Ma (Gaschnig et al., 2010); box range: 52–42 Ma
BOI-19-13	Tgd	mean of 5 grains	5 individual grains	all 40 spots	48 ± 3 Ma (Gaschnig et al., 2010); box range: 52–42 Ma

Data treatment: Dates, uncertainties, and other relevant constraints

AHe data

Treatment: (1) HeFTy: Sample mean data input to the models. Multisample sample inverse modeling with highest elevation sample for each transect as controlling sample. Run in T-Z mode. (2) QTQt: Individual grain data input to the models. Multisample sample inverse modeling for each transect.
 He dates (Ma): (1) HeFTy: Mean uncorrected He date modeled. α -ejection corrected in HeFTy using Ketcham et al. (2011). (2) QTQt: Individual grain uncorrected He date modeled. Alpha radiation damage model using Flowers et al. (2009).
 Error (Ma) applied in modeling: (1) HeFTy: The 1s sample standard deviation of uncorrected He date was applied if $\geq 10\%$. If $< 10\%$, then 10% was applied. (2) QTQt: The 1s sample analytical error of uncorrected date applied.
 r (um): (1) HeFTy: Mean equivalent spherical radius of the sample. (2) QTQt: length, width, and thickness for each individual grains, sphere (2T) as geometry.
 eU (ppm): (1) HeFTy: Mean U, Th, and Sm of the sample. (2) QTQt: U, Th, and Sm of each individual grains
 eU zonation: none assumed

Apatite fission track data (QTQt only)

Annealing model: Ketcham et al (2007)

(continued)

Table 3. Thermal History Modeling Input Table (continued)

2. Additional geologic information

(1). HeFTy Constraint

All rocks

(1) 40 °C/km geothermal gradient

(2) >3 km depth at time of emplacement

(3) 20 °C mean sea level temperature, 6.5 °C/km atmospheric lapse rate at present day.

Explanation and data source

Regional present-day geothermal gradient (Blackwell et al., 2011). Assume geothermal gradient didn't change since the placement of the rocks. Set for the model by changing basal heat flow parameter to 120 mW/m2.

Monzodiorite and granodiorite emplaced as hot magma. 3 km depth represents for 120 °C with our geothermal gradient. Emplacement dates for each sample from part 1.

Present-day approximate sea level temperature and temperature-elevation gradient

(2). QTQt Constraint

All rocks

(1) 40 ± 30 °C/km geothermal gradient, allow offset to vary over time

(2) >120 °C temperature at time of emplacement

(3) 10 ± 5 °C present day temperature, 6.5 ± 3.5 °C/km present day atmospheric gradient.

Explanation and data source

Regional present-day geothermal gradient (Blackwell et al., 2011). An anomaly high gradient of 75 °C/km in the area is also observed (Gaschnig et al., 2010). We're allowing temperature offset to change through time in QTQt model.

Monzodiorite, granodiorite, rhyolite, granite emplaced as hot magma. Emplacement dates for each sample from part 1.

Present-day approximate temperature and temperature-elevation gradient

3. System- and model-specific parameters

(1). HeFTy

Model type: Multi-sample modeling for each vertical transect. The control sample runs in time-depth (t-Z) mode. Sample stratigraphic relationship is set to nonconformity.

He kinetic model: RDAAM (Flowers et al., 2009).

Statistical fitting criteria: GOF values >0.5 for "good" fits. >0.05 for "acceptable" fits. The good-fits also must have a minimum GOF of 1/(N+1) where N is number of statistics used (Ketcham et al., 2005).

Modeling Code: AHe uses HeFTy v2.1.4

Number of tT paths attempted: 500 good paths when good paths can be found, 1000 acceptable paths otherwise, for all models.

(2). QTQt

Model type: Multi-sample modeling for each vertical transect.

Statistical fitting criteria: Newly proposed model replaces current model or gets rejected based on the acceptance function described in the Appendix A of Gallagher (2012) paper. Thermal history displayed as probability distribution of t-T paths. 95% credible intervals calculated by upper and lower 2.5% of the temperature distribution for every 1 m.y. interval (Gallagher, 2012).

Modeling Code: AHe & Apatite fission track modeled together using QTQt ver. 20210903.

Number of tT paths attempted: 400,000 burn-in and 400,000 post-burn-in for all models.

Proposal outside prior: resample proposed.

Geothermal gradient: Allow offset to vary over time.

Reheat setting: no reheating.

Model complexity: Reject more complex models that do not improve data fit.

Proposal move: Jackson Peak transect - Time: 2, Temperature: 30.0, Offset: 1; Haga Creek transect - Time: 8, Temperature: 30.0, Offset: 10; Deadwood Lookout transect - Time: 10, Temperature: 30.0, Offset: 8.

Chapter 4: Results

We report 109 new AHe dates from 21 samples (Table 2). We excluded grains with $F_i < 0.58$ or $eU < 5$ ppm due to high uncertainties associated with alpha ejection correction for these grains as they are more vulnerable to “bad neighbor” and other types of dispersion (Flowers et al., 2022b). Most samples contained 4-7 grain dates after the removal of low F_i/eU grains, except for sample BOI-21-08B, which has only 1 grain left. In addition, we applied two-sided Grubbs’ outlier test (Grubbs, 1950) at significance level of 0.005 to identify 9 grains as outliers from their sample groups. These outliers are reported in italics in Table 2, plotted in grey in Figure 3, but were excluded for sample mean calculation and were not modeled or interpreted. Possible causes for outliers can be U–Th-rich grain boundary phases (Murray et al., 2014), high eU neighbors (Speigel et al., 2009), or grooved surfaces. We reported mean sample dates with their 1σ standard deviation for samples with a coefficient of variation $<30\%$ (Table 2). Mean dates ranged from 29.9 ± 3.1 Ma to 3.9 ± 0.8 Ma. Five samples that had intrasample dispersion $>30\%$ are reported in Table 2, Figure 1, and Figure 2, but were excluded for modeling and interpretation.

Two new AFT samples’ data are reported in Supplemental Table S1 and S2. The AFT data are for sample BOI-19-11, and BOI-19-13, whose AHe dates were previously reported by Wetzel and Stanley (2022). The two samples with the new AFT dates, along with another sample, BOI-19-07, that also has AHe dates reported by Wetzel and Stanley (2022), were used for new inverse modeling.

Figure 3 shows the AHe date-eU relationship for all the samples. Most of the samples do not have a large span of eU. For the grains having a large range of eU, there is not a strong correlation between their eU and AHe dates.

South Fork Payette River cooling dates

In the Jackson Peak vertical transect at the SFPR, samples have mean AHe cooling dates from ~ 28 -9 Ma over an elevation range of 1066 m (Figure 2, Figure 4A, Table 2). This transect shows a positive date-elevation trend, with the oldest date on top of the mountain, and the youngest date at the base (Figure 4A). BOI-21-17, from the top of the Deadwood Lookout transect, 1195 m above the river level, has a mean cooling date of 29.9 ± 3.1 Ma. This transect

also has a positive date-elevation trend (Figure 4G). The river profile samples of the SFPR ranged from 25.6-3.9 Ma.

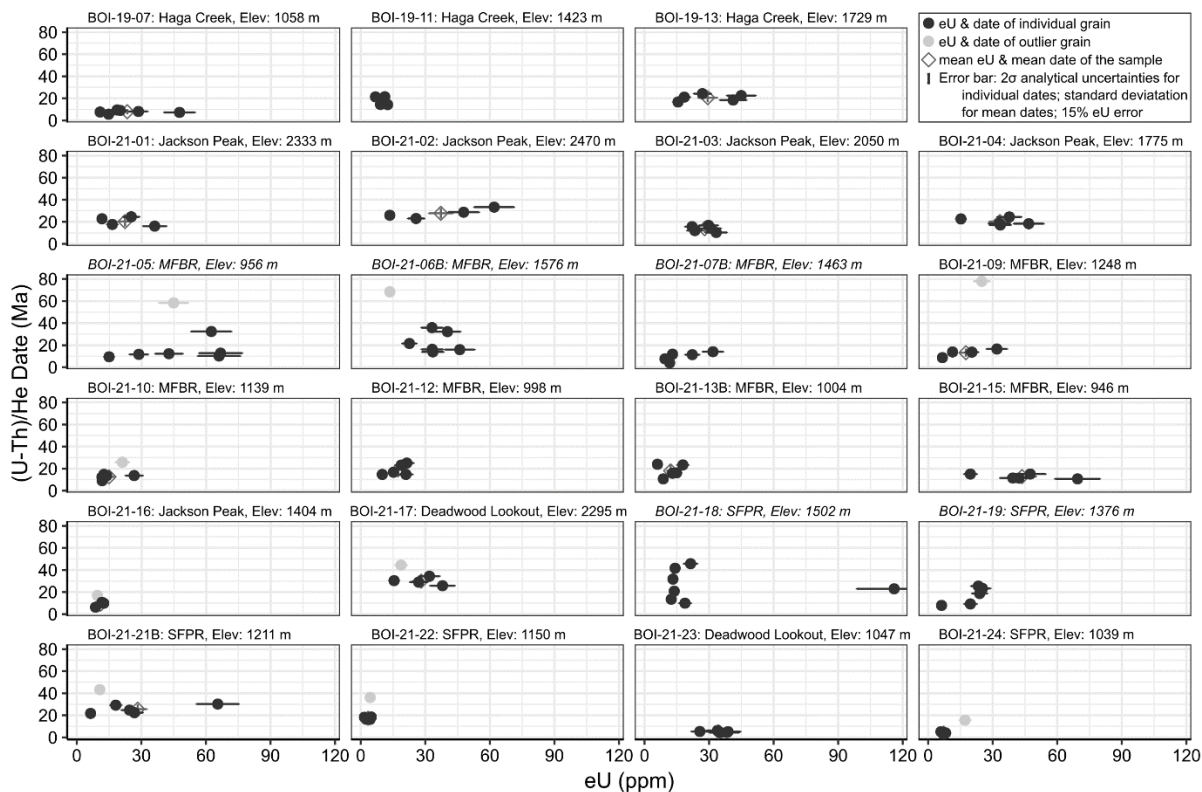


Figure 3. AHe date-eU plots of samples of this study. Individual grain eU and corrected dates are reported as black dots. Outlier grains from Grubbs' test with 0.005 significance level are reported as grey dots and are not interpreted or modeled. Errors of the grain dates are 2σ corrected analytical uncertainties and most error bars are smaller than the symbols. Errors of the grain eU are 15% of eU. For samples with dispersion <30%, sample mean eU and dates are reported as open diamonds. Errors of the sample mean dates are sample standard deviation. Errors of the sample mean eU are 15% of mean eU. Samples with dispersion >30% do not have their sample mean value reported and are labeled with italicized titles. eU-effective uranium concentration.

Middle Fork Boise River cooling dates

The new AHe mean cooling dates for the river profile samples at the MFBR range from ~19-13 Ma (Figure 2, Table 2). Samples BOI-19-13, BOI-19-11, and BOI-19-07 form the Haga Creek transect, which is also located at the MFBR and has previously been reported with mean AHe dates ranging from 20.6-7.9 Ma (Wetzel & Stanley, 2022). Positive date-elevation trend for the Haga Creek transect is observed (Figure 4D). The elevation range of the Haga Creek transect is 670 m, with the lowest sample at river level.

The new AFT data for both sample BOI-19-11 and BOI-19-13 shows Eocene cooling dates. BOI-19-11 has a central age of 37.89 ± 4.51 Ma, with $p(\chi^2) = 0.93$. BOI-19-13 has a central age of 40.7 ± 4.62 Ma, with $p(\chi^2) = 0.001$ and dispersion = $23.7 \pm 11.8\%$ (Figure 4D, Supplemental Table S1 & S2).

Inverse modeling results

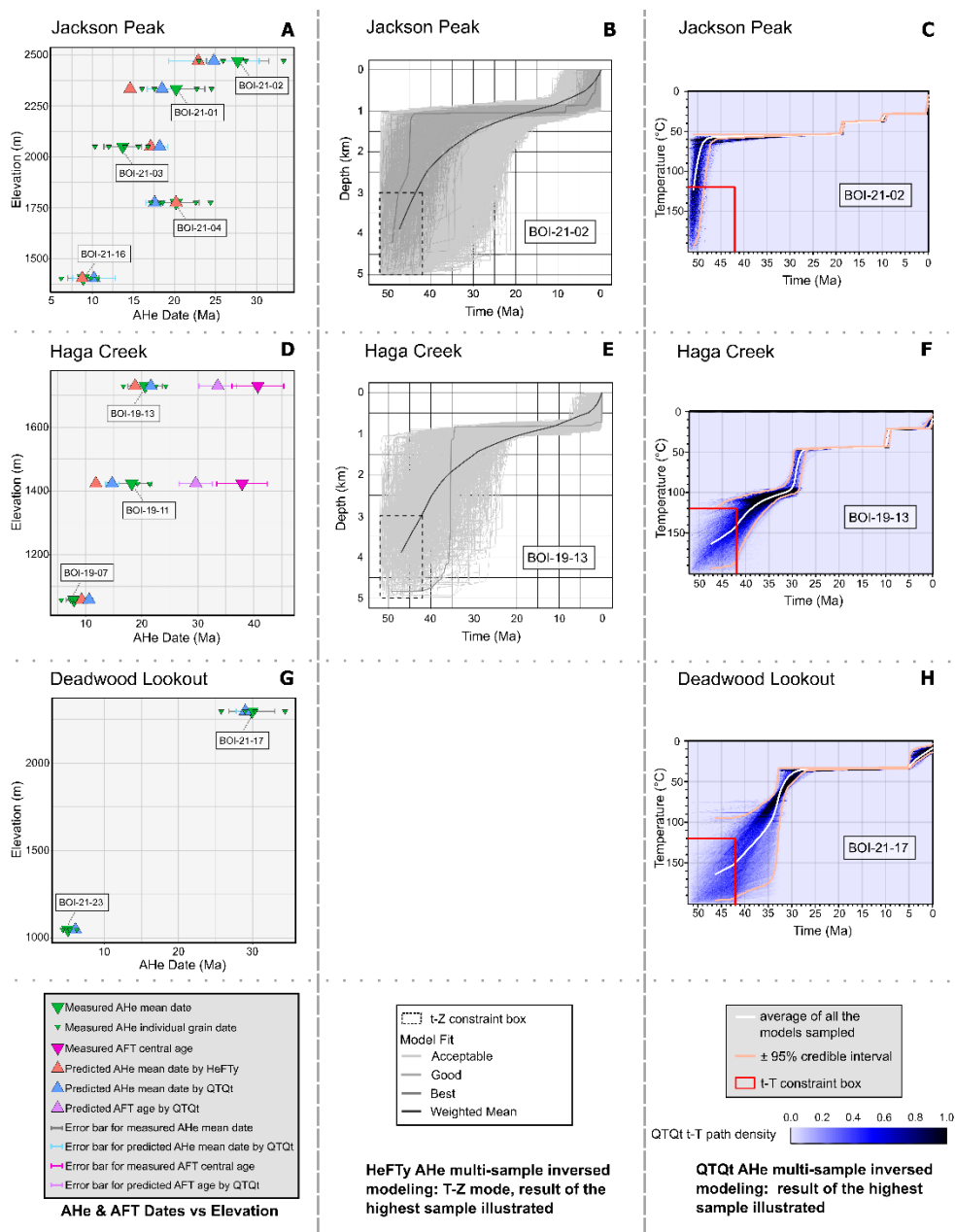
The thermal history models of the highest elevation sample (controlling sample) from each transect are plotted in Figure 4. Because the partial retention zone for the AHe system is ~30-120 °C, the data is most sensitive to this temperature range and cooling events outside this window were not interpreted.

For the Jackson Peak transect, the good-fit HeFTy models suggest that the samples cooled from >120 °C to 50-40 °C by ~40-32 Ma, followed by a long thermally stable period, until cooling below 40°C after 8 Ma (Figure 4B). The QTQt models suggest that the samples cooled to 60-55 °C no later than 45 Ma. Then a long thermally stable period extended to ~18 Ma when the samples rapidly cooled to 40 °C, followed by another stage of rapid cooling at ~10-9 Ma down to 30 °C (Figure 4C).

For the Haga Creek Transect, the HeFTy modeling could not yield any good/acceptable-fit models if both AHe dates and AFT dates are included. Because the AFT dates clearly represented rapid cooling from >120 °C in late Eocene, we only applied the AHe dates for HeFTy here to focus on the Miocene cooling pattern. By doing that, the HeFTy modeling yields acceptable-fit models (Figure 4E). These models suggest that the samples cooled from >120 °C to ~40 °C before ~25-21 Ma, followed by a thermally stable period that lasted until at least ~8 Ma followed by cooling below 30°C. The QTQt modeling, on the other hand, yields model results when both AHe and AFT are utilized, so the QTQt models for the Haga Creek contain both AHe and AFT dates (Figure 4F). The QTQt models suggest that the samples cooled from >120 °C to ~100 °C before ~42-35 Ma, then during ~30-28 Ma, the samples rapidly cooled to ~50 °C. Then the samples stayed thermally stable until ~9 Ma when they cooled below 30 °C.

For the Deadwood Transect, the HeFTy modeling does not yield any good/acceptable-fit models, so only QTQt models are presented in Figure 4H. The QTQt models suggest that the

samples cooled from >120 °C to ~ 35 °C by ~ 33 -25 Ma. Then a thermally stable period lasted until ~ 5 Ma when the samples cooled rapidly below 30 °C.



Chapter 5: Discussion

Paleogene to Oligocene Exhumation

Both HeFTy and QTQt inverse modeling results of all our vertical transects in the Boise Mountains region share two major stages of cooling with a stable period of no significant cooling in between. The discussion below is based on the cooling paths of the highest-elevation samples as they served as the controlling samples for our models (Figure 4). The first stage of cooling spans from ~50-25 Ma based on good and acceptable fit paths from HeFTy modeling with most of the good-fit paths cooling to 60-35°C by 30 Ma. This window for rapid cooling covers a large portion of the Eocene and for some models extends to Oligocene. In addition, the AFT data from the Haga Creek samples also indicates that the samples cooled below 120 °C by 40-37 Ma. This observation matches previous studies done by Sweetkind and Blackwell (1989), Fayon et al. (2017), and Wetzel and Stanley (2022), where Wetzel and Stanley (2022) suggested a Paleogene (mostly Eocene) rapid exhumation period in the broad southern Idaho batholith region based on thermochronometers they used that range in closure temperatures from 250-30 °C, with most samples crystallizing during late Cretaceous but all have Eocene cooling dates (Figure 1). This supports that the cooling signals we observe in our samples are most likely reflecting the Eocene exhumation events instead of reflecting post-magmatic isobaric cooling of the samples following emplacement, although Eocene cooling may reflect a combination of exhumation and post-magmatic cooling. Below we discuss the potential causes of this Eocene rapid exhumation phase.

Multiple factors from previous studies suggested that the Idaho batholith was a crustal plateau prior to Challis magmatism, at least since the emplacement of the Atlanta lobe (Figure 5A). These factors include that the peraluminous suite of Atlanta Lobe is largely sourced from crustal melts formed in overthickened crust (Gaschnig et al., 2011; Davenport et al., 2017); sediment sourced from Idaho batholith is found in Paleogene basins across Alaska (71–65 Ma, Dumitru et al., 2016), California (53–37 Ma, Dumitru et al., 2013), Nevada (49-39 Ma, Canada et al., 2019), Oregon (49 to 36 Ma, Dumitru et al., 2013; Eocene, Heller et al., 1985), Wyoming (~50–47 Ma, Dumitru et al., 2013 and Chetel et al., 2011), and Washington (91–75 Ma, Dumitru et al., 2016; Mid Eocene, Heller et al., 1985 and Wells 1989); the Idaho batholith is isotropic on a regional scale without strong Cretaceous fabrics suggesting neutral to

extensional crustal plateau tectonic setting during placement (Giorgis et al., 2006; Byerly et al., 2017); and fossil leaves (Wolfe et al., 1998) and δD of paleo-meteoric water contained in volcanic glass (Cassel et al., 2014) both suggest that the elevation of central Idaho was much higher in the Paleogene than today (Figure 5A). However, being a topographic high during the late Cretaceous and Paleogene does not necessarily guarantee high erosion rates if the plateau interior remained low relief. Fayon et al. (2017) suggested based on zircon (U-Th)/He data that the region was thermally stable prior to the Challis magmatism, which would indicate a low erosion rate. Most of the Idaho batholith detrital sediment records in Paleogene basins mentioned above were deposited post Challis magmatism, also suggesting that the erosion rate increased after Challis magmatism. In addition, Wetzel and Stanley (2022)'s and our new data all support that there was a major exhumation event that occurred after Challis magmatism. Although our data and models cannot constrain when Eocene exhumation began, we do show rapid exhumation after Challis magmatism and suggest that mechanisms associated with Challis magmatism dramatically increased the relief and erosion rate in the area (Figure 5B).

The Challis magmatism (51 Ma to 43 Ma, Gaschnig et al., 2010) has been attributed to the extensional collapse of overthickened crust, potentially triggered by decreased plate convergence rate at the western North American margin, or Farallon slab roll back (Figure 5B) (Humphreys, 1995; Constenius, 1996; Gaschnig et al., 2011). Early extensional features in the region are NE striking, high angle, normal fault systems active during the peak of Challis magmatism at about 49-48 Ma with offsets up to a few kilometers (Janecke 1992). Within our study area, these features are part of the Trans-Challis Fault Zone (TCFZ, Figure 1). TCFZ contains numerous NE striking faults, covers multiple Challis eruptive centers, and extends through central Idaho (Bennett, 1980; Bennett, 1986). These NE striking faults could have led to fault-driven exhumation during Challis volcanism and increased the regional relief, resulting in a higher erosion rate over a longer term (Figure 5B).

There is also evidence from stable isotopes for surface uplift during Challis magmatism either due to thermal effects of upwelling asthenosphere through a slab window or delimitation beneath the batholith (Figure 5B) (Humphreys, 1995; Breitsprecher et al., 2003; Kent-Corson et al., 2006; Duke 2009; Gaschnig et al., 2011; Cassel et al., 2018). The reduction in $\delta^{18}O$ indicates a 2.5-3.5 km elevation increase in the region (Kent-Corson et al., 2006). Such an

uplift would have caused a corresponding increase in relief and erosion rates, supported by the rapid cooling seen in our data.

Our new AFT dates and new vertical transect modeling from new and preexisting thermochronology suggest a high erosional rate from high-relief topography, or high exhumation rate from extensional faults, or a combination of both, for the Boise Mountains from the time of Challis magmatism to the Oligocene. This picture matches well into the popular model of collapsing over-thickened plateau, potentially with a slab window created underneath either by Farallon slab rollback or ridge subduction (Breitsprecher et al., 2003; Gaschning et al., 2011; Schmandt & Humphrey, 2011; Byerly et al., 2017; Fayon et al., 2017). Our data do not show a relief reduction in Oligocene that is seen in the Owyhee Mountains south of the WSRP (Wetzel & Stanley, 2022), suggesting perhaps high relief topography persisted longer in the Boise Mountains than in the Owyhee Mountains.

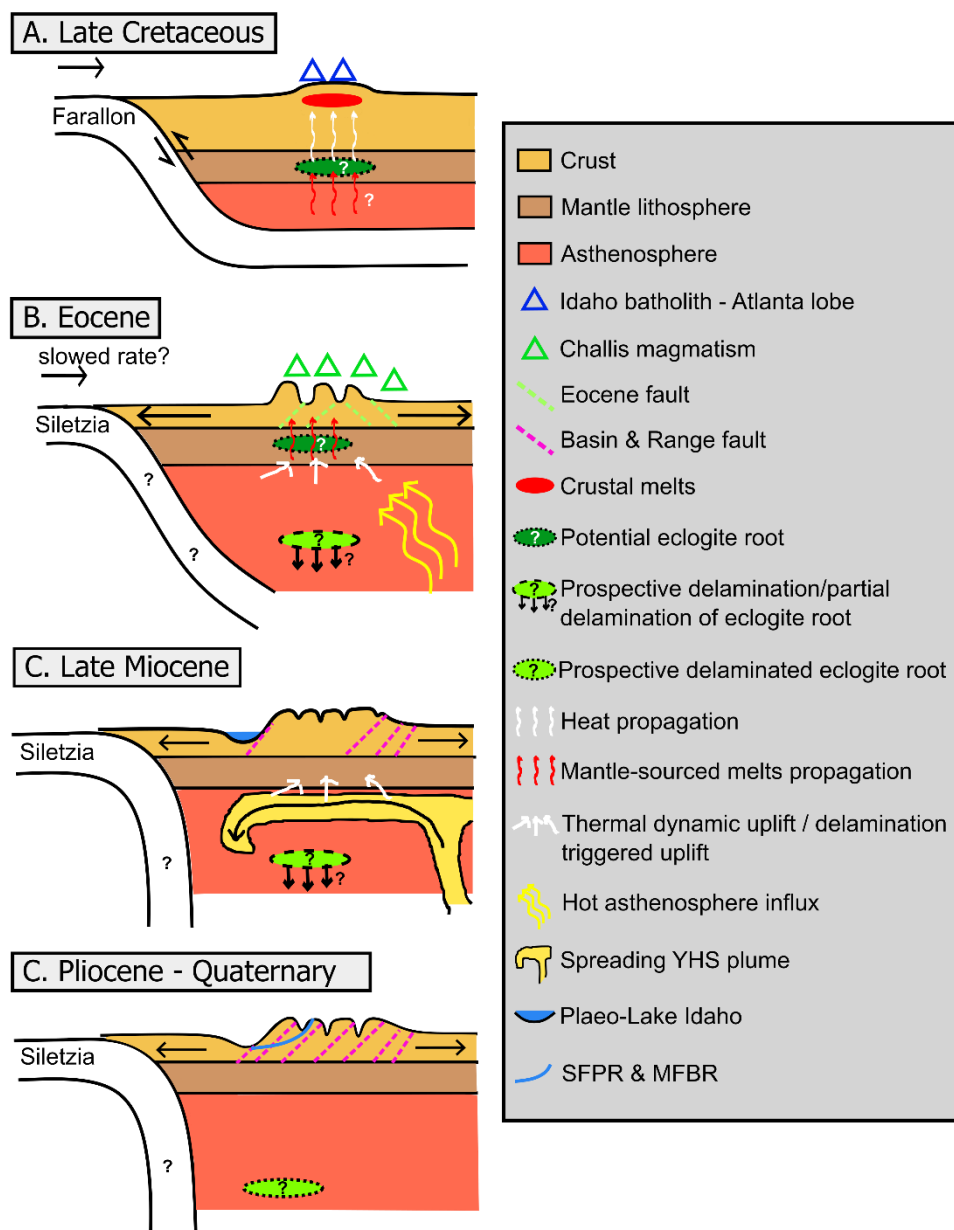


Figure 5. Schematic cross section across the southern Atlanta lobe of Idaho batholith illustrating the tectonic model for Cenozoic exhumation at the Boise Mountains based on our AHe and AFT data and other geologic evidence. Approximate cross section location shown in Figure 1 inset. (A). Late Cretaceous: Thickened crust plateau during the eruption of the Atlanta lobe of Idaho batholith, which is sourced from crustal melts. (B). Eocene: Collapsing of the overthickened plateau in extensional setting and potential opening of slab window leads to Challis magmatism. The influx of hot asthenosphere from the slab window opening can lead to thermal dynamic uplift, and potentially trigger partial delamination of dense eclogite root under the Boise Mountains which would also lead to uplift, resulting in higher relief and increased erosional rate. Crustal extension leads to the formation of Eocene normal faults including the Trans Challis fault zone. (C). Late Miocene: The spreading of the Yellowstone hotspot plume can lead to thermal dynamic uplift. The return flow of the plume near the craton boundary can potentially cause delamination of the rest of dense eclogite root beneath the Boise Mountains, which also leads to uplift and allows Basin and Range faults to propagate to the southern Atlanta lobe. The uplift results in increased relief and erosion rate. The Western Snake River Plain is filled by the paleo-Lake Idaho. (D). Pliocene – Quaternary: The draining of paleo-Lake Idaho leads to incision of the South Fork Payette River and the North Fork Boise River. Young Basin and Range faults cutting the river profile and disrupting isochrones. Delaminated eclogite root and potential remnant of rolled-back Farallon plate form the seismic high-velocity field.

Late Miocene Rejuvenation

The second major cooling stage shared in both HeFTy and QTQt models for all our vertical transects is in late Miocene. The highest-elevation samples of each transect cooled from 50-35 °C to present day temperature between 10 Ma and today (Figure 4). There is a rapid cooling signal from 60-55 °C down to 40 °C at ~18 Ma in the QTQt model for the Jackson Peak transect (Figure 4C), but this cooling event is not observed in the HeFTy models for this transect nor any other models for other transects (Figure 4 E-H), so we tend to not consider it representative of a regional cooling signal. Based on thermal history models, the beginning of the regional second cooling stage was in late Miocene, and potentially extended to the Quaternary but it is hard to determine due to the insensitivity of AHe system below 30 °C. Between 10 Ma and today, the HeFTy models suggest ~0.85-0.7 km exhumation for the highest sample with 40 °C geothermal gradient. The QTQt models suggest ~1.6-1 km exhumation with ~25-16 °C contemporary geothermal gradient for the highest samples. This cooling phase matches the suggestion of late-Miocene landscape rejuvenation and rapid exhumation in the Boise Mountains from previous studies. Considering that the vertical transects have ~1-0.7 km elevation offset, samples at the bottom of the river valley could have up to ~2.6 km exhumation during this time. This is close to the AFT and ZFT studies that suggested a maximum of 3 km exhumation since <10 Ma at the bottom of some of the deepest river valleys of the region (Sweetkind and Blackwell, 1989). It is also in line with river geomorphology studies in central Idaho that suggested increased incision since 13-8 Ma caused by northward tilting uplift (Larimer et al., 2018; Mitchell & Yanites, 2019), and the relict surfaces that suggested plateau dissection from late Miocene to Pliocene (Blackwelder, 1912).

The cooling history from our models suggests a long period of time in the PRZ, but this is not reflected in the date-eU relationship as shown in Figure 3. We suggest that this is due to the lack of a large eU span in many of our samples and the lack of enough grains for each sample to show the date-eU correlation.

Looking back to the hypotheses we proposed (Table 1), the CRB-triggered exhumation requires regional rapid cooling starting from 16 Ma, which we do not see in most of our models except for a minor cooling step in the QTQt model for the Jackson Peak transect that we do not consider a regional pattern. We therefore do not favor the CRB eruption to be the major

cause of Miocene exhumation. The Yellowstone hotspot triggered thermodynamic uplift and/or delamination requires a regional exhumation signal from ~11-8 Ma, which matches the rapid cooling window from the models. We therefore consider Yellowstone-related mechanisms to be a viable trigger for Miocene exhumation. For the Basin and Range faulting-caused exhumation to be the major driving factor, rapid exhumation signals would be expected adjacent to faults that have large offsets. However, we observe a regional rapid exhumation pattern without obvious differences across faults. In addition, reported by Wetzel and Stanley (2022), the AHe samples from the Bogus Basin transect that are located at the footwall side of the basin-bounding Boise Front fault system all have Eocene cooling ages, showing that the exhumation from this fault was limited. We therefore consider Basin and Range faulting unlikely to be the major factor causing Miocene rejuvenation, though more data focused around specific faults might be needed to fully rule out this mechanism. For Miocene exhumation driven by base-level drop and enhanced river incision to be the major factor, the rapid exhumation needs to match the enhanced river incision period during 16-9 Ma if caused by the extension and subsidence of WSRP, and/or during ~4 Ma to present day if caused by the draining of the paleo-Lake Idaho. We do see rapid exhumation from 11-8 Ma which would be consistent with this, but based on the evidence from our horizontal transects' cooling dates, we propose that the rapid exhumation was prior to the major river incision period, which we will discuss in detail in the next section. Among all the hypotheses we proposed, the Yellowstone hotspot-related hypothesis is most likely to be the major cause of the rapid Miocene exhumation, though Basin and Range faulting and river incision due to base level drop in the WSRP may have enhanced exhumation.

The timing for the start of this Miocene rejuvenation in our models is contemporaneous with the timing for the establishment of the Twin Falls volcanic field (10.9-8.6 Ma) and the Picabo volcanic field (10.3-8.2 Ma) (Pierce & Morgan, 1992; Bonnicksen et al., 2008; Vogl et al., 2014). Both volcanic fields are close to the Boise Mountains, located south to southeast of the Atlanta lobe, on the ESRP (Figure 1). Rock uplift driven by the approaching hotspot could be the cause of the exhumation in the Boise Mountains. Closer to the ESRP in the Pioneer Mountains (Figure 1), 2-3 km of rapid exhumation since 11 Ma based on AHe data has been attributed to a combination of thermal dynamic uplift and flexural uplift caused by the passage of the hotspot (Vogl et al., 2014). Flexural effects of loading and subsidence in the ESRP are

limited to close proximity to the ESRP (McQuarrie & Rodgers, 1998) so we do not expect this to be affecting our study region, but thermal-dynamic uplift might have played a role. Our observations are compatible with and support the northward tilting model proposed by Larimer et al. (2018) and Mitchell and Yanites (2019), because the thermal dynamic effect will decay towards north as it gets further away from the plume. In addition, Larimer et al. (2018) showed that such a model with greater rock uplift in the south tapering to the north could be caused by a buried buoyant load that could be either due to thermal change or delamination in the mantle lithosphere.

Several lines of evidence suggest that the northern Atlanta lobe has a deep crustal root at present, while the southern Atlanta lobe does not. (1). Seismic studies show high velocity structures of a vertically oriented curtain and blobs underlying the Atlanta lobe, while the area below WSRP, ESRP, and east central Idaho have relatively low velocity (Roth et al., 2008; Tian & Zhao, 2012). The curtain is suggested to be the remnant of a subducted plate (Schmandt & Humphrey, 2011), while the blobs can be eclogite roots beneath the batholith. The north part of the Atlanta lobe has a blob directly attached to the bottom of the Moho, possibly representing that the eclogite root is still attached to the crust at north. However, in the southern part of the batholith, the blob appears to be detached from the crust and located at 200-300 km depth (Roth et al., 2008), and this could represent the delaminated dense root from the southern Atlanta lobe. (2). Tikoff et al. (2001) and Ruppel (1982)'s study noted that much of the NW striking, SW dipping Basin and Range faults in the WISZ and east central Idaho could be reactivated old lithospheric and crustal structures. Similar faults are also extensive across the southern Atlanta lobe (Bennett, 1980; Bennett, 1986; Breckenridge et al., 2003). However, in the northern Atlanta lobe, there are no pervasive large young faults, and for those that exist, their orientation is not consistent, and their offset is limited (Hamilton, 1963; Breckenridge et al., 2003). Tikoff et al. (2001) attributed this to the existence of a dense crustal root attached beneath the northern Atlanta lobe that inhibited the reactivation of old structures at depth. And we speculate that the southern part of the Atlanta lobe has been much more affected by Basin and Range and younger faulting because the eclogite root has delaminated. (3). Modern GPS suggests clockwise rotation of multiple regional crustal blocks, including the southern Atlanta lobe, around a rotation pole in the northern Idaho batholith (Payne et al., 2012; McCaffrey et al., 2013). It has been suggested that the deep root in the northern part is anchoring it, which

does not appear to be happening in the south (McCaffrey et al., 2013).

There are two common ways to form dense eclogite crustal roots. One is to form eclogite facies metamorphic rock from preexisting crustal rock sequences through solid state metamorphic reactions during crustal thickening (Saleeby et al., 2003). The other way is to segregate garnet-pyroxene residues through crystal-liquid equilibria during the formation of felsic batholithic rocks (Saleeby et al., 2003). According to this, we propose two possible timings for the dense root to have formed. One possible time window is in Cretaceous during the compressional tectonic setting when the crust was thickened and formed the plateau at Idaho (Figure 5A). The other window is during the Challis magmatism when partial melting at mantle lithosphere occurred either due to decompression or extension or the heat released from ascending hot asthenosphere through slab window (Figure 5B) (Norman & Mertzman, 1991; McKervery, 1998; Gasching et al., 2011). Our data are not related to how a dense root was formed and cannot distinguish between these mechanisms.

From our AHe data, there are two periods of rapid exhumation, one at Eocene to late Oligocene, the other at late Miocene to Pliocene. Because delamination will result in regional rock uplift and thus increase erosional rate, it could occur in either of the rapid exhumation periods observed above. For the Eocene period, if slab window had occurred during the Challis magmatism, the influx of the hot asthenosphere could decouple the dense eclogite from the rest of the crust (Figure 5B) (Humphreys, 1995; Cassel et al., 2018). As for late Miocene period, Burov et al. (2007)'s research shows that a spreading plume will have a return flow near the boundary between a craton and younger lithosphere and cause vertical down-thrusting of mantle lithosphere, leading to delamination of dense roots. The Boise Mountains are located close to the Mesozoic continental margin between the old North American Craton to the east and the young oceanic accreted terrain to the west (Figure 1). The plume of the Yellowstone hotspot could have spread from the Twin Falls and Picabo volcanic fields across the Boise Mountains towards the continental margin during late Miocene and formed return flow close to the boundary while causing delamination (Figure 5C). During which of the two periods the delamination occurred is beyond the scope of what our data can reveal. However, as the dense root beneath the northern Atlanta lobe appears to still exist at present while the root beneath the Boise Mountains does not, we prefer the late Miocene delamination scenario caused by the

Yellowstone hotspot, for two reasons. (1). The close proximity of the Yellowstone hotspot to the Boise Mountains relative to the northern Atlanta lobe (Figure 1) could explain this heterogeneous delamination (2). The Challis magmatism was extensive across the whole batholith and therefore cannot explain the heterogeneity. If there was delamination during Eocene, we hypothesize that the delamination intensity is limited, with most of the dense root retained. Alternatively, intensive Eocene delamination may have removed the root from the whole Atlanta lobe, and the subducted Farallon Plate (Schmandt & Humphrey, 2011) is solely serving as the lithospheric keel for the northern Atlanta lobe.

Pliocene to Quaternary River Incision and Basin and Range Faults Disturbance

From the date-river profile plot we can divide the samples into segments for both rivers (Figure 6A, 6B). Within each segment, the samples get older upstream, but between each segment there is a sudden jump in the cooling dates (Figure 6A, 6B). We infer that the segments are split where young faults offset the original trend of dates. In order to generate such a date-river profile relationship, the river incision must have occurred after the samples cooled below the closure temperature. Using SFPR as an example for the incision model (Figure 6C), we assumed that the AHe date isochrones (surfaces of equal cooling date, e.g., McPhillips & Brandon 2010) were horizontal prior to the river incision (top of Figure 6C). As the river topography started to retreat, it would bend the closure temperature isotherm towards downstream (middle of Figure 6C). If the samples cooled below the closure temperature during or immediately after the incision, their isochrones would be bent with the isotherm and would result in a younger trend towards upstream within each segment, unlike what we observe in Figure 6A and 6B. Conversely, if the samples already cooled below the closure temperature, their isochrones would stay horizontal (middle of Figure 6C), which would result in the older-upstream trend that we observe (Figure 6A and 6B). If faults were active after the major exhumation period, the faults would also offset the sample isochrones, resulting in age segments along the river profile, and the samples would be older upstream within each segment (bottom of Figure 6C), as we observe in our data. We suggest that this most recent incision was caused by the downstream base level drop from the draining of the paleo-Lake Idaho, which lasted from ~4 Ma to late Quaternary with a lake level decline rate of 120 m/Ma (Wood & Clemens, 2002). This time is well past the start of the late Miocene rapid cooling period indicated by our models at 10 Ma, leaving enough time for the samples to cool below the

closure temperature (Figure 5C to 5D). The draining and demise of the paleo-Lake Idaho helped to carve Hells Canyon downstream, proving it had enough impact to cause river incision (Wood & Clemens, 2002; Kahn et al., 2020). We speculate that Basin and Range faults offset the river and disrupted the pattern of sample dates (Figure 6). For the SFPR transect, between sample BOI-21-16 and BOI-21-21B, there are the Bear River fault and the Deer Park fault (Figure 2 and Figure 6A), both of which were SW dipping normal faults active since 16 Ma (Breckenridge, 2003). Activity on these faults after major exhumation period would bring samples with younger cooling dates up to the river level on the upstream/footwall side of the fault (bottom of Figure 6C), for example, explaining why BOI-21-16 has a much younger date than BOI-21-21B (Figure 6A). Between sample BOI-21-22 and BOI-21-23, the Deadwood fault system (Figure 2 and Figure 6A) is composed of east dipping normal faults active since 1.6 Ma (Breckenridge, 2003). The orientation of this fault system would bring samples with younger cooling dates up to the river level in the downstream direction (bottom of Figure 6C), explaining why BOI-21-23 is much younger than BOI-21-22 despite minimal difference in elevation. We suggest a similar mechanism of fault segmentation can explain the pattern of dates for the MFBR samples (Figure 6A), though the faults are not as well constrained in this area and there may be unidentified faults (Kiilsgaard et al., 2001; Breckenridge, 2003; Kiilsgaard et al., 2006).

A caveat for this model is that it cannot tell whether the faults occurred before, during, or after the river incision. Although in the Figure 6 we assume the situation of flat initial isochrones prior to the river incision for illustration, the more precise description of the model requirement is that the isochrones must be flat before faulting, and the faulting that resulted in offset horizontal isochrones could occur prior to the incision. As long as the faults offset the isochrones after the major exhumation period (in our case, < 11-8 Ma), the resulting pattern will be similar. Another limit of this model is that currently this observation of the date-river transect pattern is more focused on downstream, especially for the MFBR. If we had more upstream samples that were not over-dispersed, we could tell whether the same pattern occurred upstream too and examine whether this model is able to explain the entire incision process of the rivers. Because many of the samples with dispersion <30% that we have are downstream, there is an alternative model that can explain the pattern too. The alternative model is that the rapid exhumation occurred long after the major incision event was completed,

so that the isotherms at downstream area had returned to near flat before samples cooled below the AHe closure temperature. In this case the sample dates would also show the pattern of being older towards upstream, and the young faults could cause the segmentation of dates. However, this would require the incision to occur well before the cooling dates of the river samples. From Figure 6 we can see that some samples have cooling dates > 16 Ma, which are older than both of our hypothesized Miocene-Pliocene mechanisms that can trigger river incision (Table 1). Although we cannot deny the possibility of other Miocene-Pliocene mechanisms causing the early river incision, such early incision, if occurred, would likely be during Eocene extension, which makes us not favor this alternative model because all our sample dates are Miocene or younger. Overall, based on our new AHe dates from the horizontal transect samples along the SFPR and the MFBR, we speculate that the river incision of the modern channel started after the samples cooled below the closure temperature, possibly $< \sim 4$ Ma, and was triggered by the draining of the paleo-Lake Idaho. The sample dates were disturbed by young Basin and Range faults that offset the channel after the major late Miocene-Pliocene exhumation (Figure 5D).

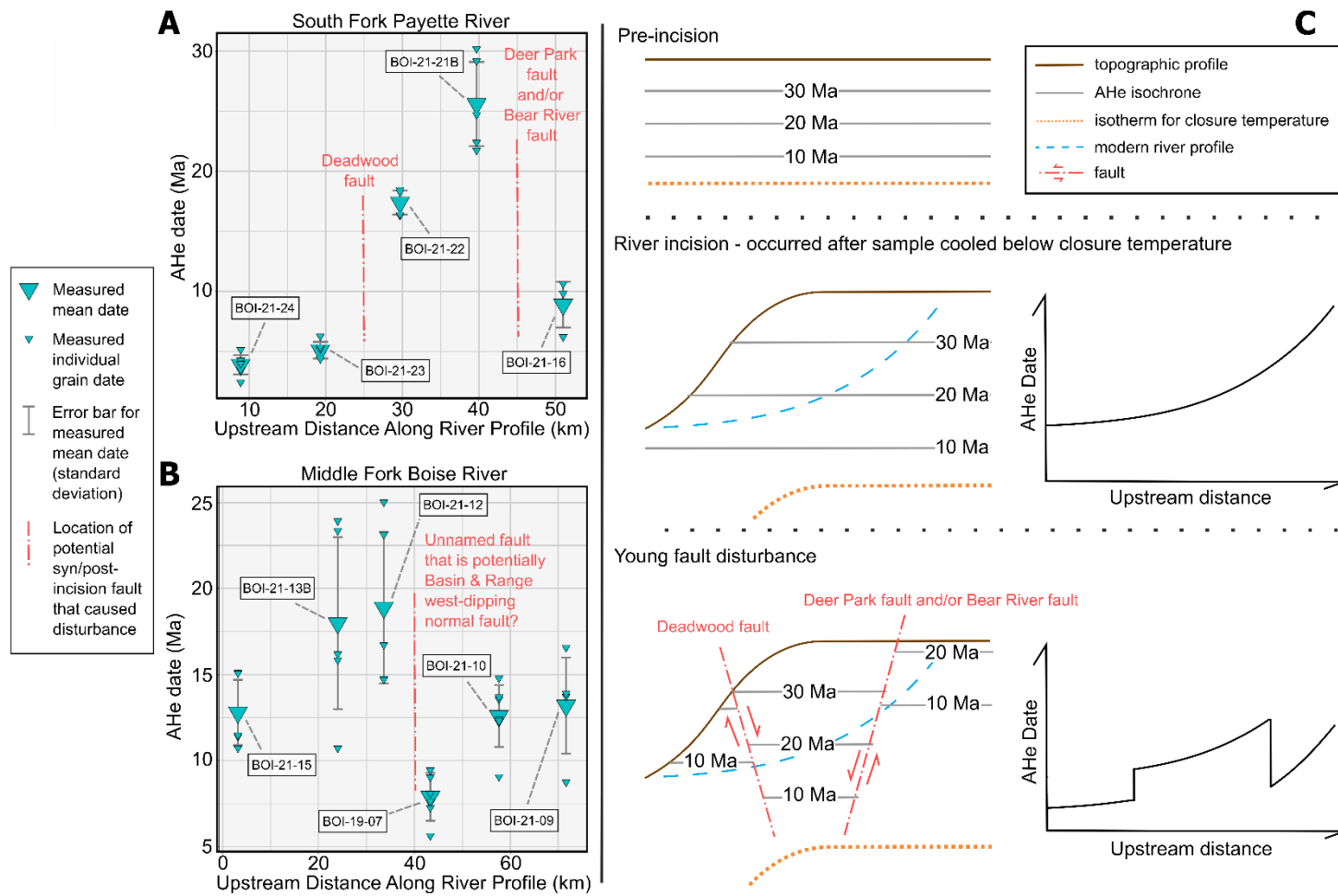


Figure 6. (1). AHe date-river profile for samples located at river level along the South Fork Payette River (A) and Middle Fork Boise River (B). The cooling dates of individual grains and sample mean are shown. The error bar of the sample mean date is the standard deviation. Faults that potentially affected the sample date pattern are plotted at their corresponding upstream distance along the river profile. Locations of the faults are in Figure 2. (2). River incision model to explain the AHe date-river profile pattern using the South Fork Payette River as an example. Isochrones here are surfaces of equal AHe cooling dates. Initially flat isochrones are assumed. The curved topographic profiles in the lower two plots represent contemporary river profiles. Isotherm for closure temperature bends in response to the river incision, but because the samples have cooled below the closure temperature before the incision, the related isochrones do not bend. See text for more explanation. The model is modified from Schildgen et al. (2007).

Chapter 6: Conclusions

Our new AHe and AFT dates from the MFBR and SFPR in the Boise Mountains indicate a two-stage rapid cooling pattern during Eocene-Oligocene and late Miocene–Pliocene. Thermal history inverse modeling of the Jackson Peak, Haga Creek, and Deadwood Lookout vertical transects suggest that during Eocene-Oligocene period, the Boise Mountains experienced rapid exhumation that brought samples to $< \sim 2.6$ km depth followed by a long period of thermally stability, until late Miocene. During late Miocene-Pliocene, at least ~ 0.7 km exhumation occurred in the region. From Pliocene to Quaternary, river incision carved the deep valleys for the SFPR and MFBR.

The Eocene–Oligocene rapid exhumation matches previous thermochronology studies in the Idaho Batholith that yielded Eocene cooling dates across the Atlanta lobe (e.g., Sweetkind & Blackwell, 1989; Wetzel and Stanley, 2022). Together they show substantial cooling and exhumation associated with the Challis magmatism and extension that could be due to multiple processes. The influx of hot asthenosphere through a slab window (e.g., Gaschnig et al., 2011) could have caused regional rock uplift and exhumation due to thermal dynamic processes and/or delamination, in addition to triggering Challis magmatism (e.g., Humphreys, 1995; Cassel et al., 2018). Extensional faulting such as the NE trending TCFZ could have contributed to the exhumation. The modeled exhumation period extended to Oligocene, indicating that the regional exhumation continued after the Challis magmatism had ceased.

The start timing of the late Miocene–Pliocene rapid exhumation is temporally coincident with the 11-8 Ma Yellowstone hotspot Volcanism at the Twin Falls and Picabo volcanic fields to the south of the Boise Mountains. The magnitude of exhumation in the Boise Mountains combined with other erosion history data from cosmogenic radionuclide and geomorphic studies suggests more erosion and rock uplift in the southern Atlanta lobe than the north (Larimer et al., 2018; Mitchell & Yanites, 2019). We suggest that the nearby existence of the plume caused thermal dynamic uplift and/or delamination under the Boise Mountains, resulting in increased erosion rate and leading to the rapid exhumation. Thermal dynamic effects would have decayed northward with increased distance from the hotspot, providing a mechanism for the spatial pattern in rock uplift. Delamination could have been triggered by the return flow of the spreading plume (Burov et al., 2007), only affecting the nearby southern portion of the Atlanta

lobe, which is supported by the seismic studies which showed that the northern Atlanta lobe maintained a deep lithospheric root while the southern portion did not (Roth et al., 2008; Tian & Zhao, 2012). While delamination could have occurred during the Eocene exhumation period, the Miocene exhumation period, or both, delamination initiated by the hotspot during the Miocene provides a mechanism for the localization of rock uplift and root removal in the south of the Atlanta lobe.

The pattern of cooling dates in our river-level samples, together with the location and orientation of the post-Miocene Basin and Range faults, suggest that the incision of the modern MFBR and SFPR started after the samples cooled below the closure temperature. We propose that the draining of the paleo-Lake Idaho since ~4 Ma enhanced the river incision. The recent faults offset channels post the late Miocene exhumation, disturbing the AHe dates and potentially augmenting incision.

References

- Anderson, A.L., 1952, Multiple Emplacement of the Idaho Batholith: *The Journal of Geology*, v. 60, p. 255–265, doi:10.1086/625961.
- Ault, A.K., Gautheron, C., and King, G.E., 2019, Innovations in (U–Th)/He, Fission Track, and Trapped Charge Thermochronometry with Applications to Earthquakes, Weathering, Surface-Mantle Connections, and the Growth and Decay of Mountains: *Tectonics*, v. 38, p. 3705–3739, doi:10.1029/2018TC005312.
- Bennett, E.H., 1980, Reconnaissance Geology and Geochemistry of the Trinity Mountain-Steel Mountain Area, Elmore County, Idaho: Idaho Geological Survey Technical Reports T-80-11, scale: 1:63,360.
- Bennett, E.H., 1986, Relationship of the trans-Challis fault system in central Idaho to Eocene and Basin and Range extensions: *Geology*, v. 14, p. 481–484, doi:10.1130/0091-7613(1986)14<481:ROTTFS>2.0.CO;2.
- Bezanson, J., Edelman, A., Karpinski, S., and Shah, V.B., 2017, Julia: A fresh approach to numerical computing: *SIAM Review*, v. 59, p. 65–98, doi:10.1137/141000671.
- Blackwelder, E., 1912, The Old Erosion Surface in Idaho: A Criticism: *The Journal of Geology*, v. 20, p. 410–414, doi:10.1086/621986.
- Bonnichsen, B., Leeman, W.P., Honjo, N., McIntosh, W.C., and Godchaux, M.M., 2008, Miocene silicic volcanism in southwestern Idaho: geochronology, geochemistry, and evolution of the central Snake River Plain: *Bulletin of Volcanology*, v. 70, p. 315–342, doi:10.1007/s00445-007-0141-6.
- Braun, J., 2002, Quantifying the effect of recent relief changes on age–elevation relationships: *Earth and Planetary Science Letters*, v. 200, p. 331–343, doi:10.1016/S0012-821X(02)00638-6.
- Breckenridge, R.M., Lewis, R.S., Adema, G.W., and Weisz, D.W., 2003, Miocene and younger faults in Idaho: Idaho Geological Survey, Map 8
- Breitsprecher, K., Thorkelson, D.J., Groome, W.G., and Dostal, J., 2003, Geochemical confirmation of the Kula-Farallon slab window beneath the Pacific Northwest in Eocene time: *Geology*, v. 31, p. 351–354, doi:10.1130/0091-7613(2003)031<0351:GCOTKF>2.0.CO;2.

- Burov, E., Guillou-Frottier, L., d'Acremont, E., Le Pourhiet, L., and Cloetingh, S., 2007, Plume head–lithosphere interactions near intra-continental plate boundaries: *Tectonophysics*, v. 434, p. 15–38, doi:10.1016/j.tecto.2007.01.002.
- Byerly, A., Tikoff, B., Kahn, M., Jicha, B., Gaschnig, R., and Fayon, A.K., 2017, Internal fabrics of the Idaho batholith, USA: *Lithosphere*, v. 9, p. 283–298, doi:10.1130/L551.1.
- Camp, V.E., 2013, Origin of Columbia River Basalt: Passive rise of shallow mantle, or active upwelling of a deep-mantle plume?, *in* Reidel, S.P., Camp, V.E., Ross, M.E., Wolff, J.A., Martin, B.S., Tolan, T.L., and Wells, R.E. eds., *The Columbia River Flood Basalt Province*, Geological Society of America, v. 497, p. 0, doi:10.1130/2013.2497(07).
- Camp, V.E., and Ross, M.E., 2004, Mantle dynamics and genesis of mafic magmatism in the intermontane Pacific Northwest: *Journal of Geophysical Research: Solid Earth*, v. 109, doi:10.1029/2003JB002838.
- Canada, A.S., Cassel, E.J., Stockli, D.F., Smith, M.E., Jicha, B.R., and Singer, B.S., 2019, Accelerating exhumation in the Eocene North American Cordilleran hinterland: Implications from detrital zircon (U-Th)/(He-Pb) double dating: *GSA Bulletin*, v. 132, p. 198–214, doi:10.1130/B35160.1.
- Cassel, E.J., Breecker, D.O., Henry, C.D., Larson, T.E., and Stockli, D.F., 2014, Profile of a paleo-orogen: High topography across the present-day Basin and Range from 40 to 23 Ma: *Geology*, v. 42, p. 1007–1010, doi:10.1130/G35924.1.
- Cassel, E.J., Smith, M.E., and Jicha, B.R., 2018, The Impact of Slab Rollback on Earth's Surface: Uplift and Extension in the Hinterland of the North American Cordillera: *Geophysical Research Letters*, v. 45, p. 10,996–11,004, doi:10.1029/2018GL079887.
- Chetel, L.M., Janecke, S.U., Carroll, A.R., Beard, B.L., Johnson, C.M., and Singer, B.S., 2011, Paleogeographic reconstruction of the Eocene Idaho River, North American Cordillera: *GSA Bulletin*, v. 123, p. 71–88, doi:10.1130/B30213.1.
- Constenius, K.N., 1996, Late Paleogene extensional collapse of the Cordilleran foreland fold and thrust belt: *GSA Bulletin*, v. 108, p. 20–39, doi:10.1130/0016-7606(1996)108<0020:LPECOT>2.3.CO;2.
- Cooperdock, E.H.G., Ketcham, R.A., and Stockli, D.F., 2019, Resolving the effects of 2-D versus 3-D grain measurements on apatite (U–Th)\,He age data and reproducibility: *Geochronology*, v. 1, p. 17–41, doi:10.5194/gchron-1-17-2019.

- Criss, R.E., Lanphere, M.A., and Taylor Jr., H.P., 1982, Effects of regional uplift, deformation, and meteoric-hydrothermal metamorphism on K-Ar ages of biotites in the southern half of the Idaho Batholith: *Journal of Geophysical Research: Solid Earth*, v. 87, p. 7029–7046, doi:10.1029/JB087iB08p07029.
- Davenport, K.K., Hole, J.A., Tikoff, B., Russo, R.M., and Harder, S.H., 2017, A strong contrast in crustal architecture from accreted terranes to craton, constrained by controlled-source seismic data in Idaho and eastern Oregon: *Lithosphere*, v. 9, p. 325–340, doi:10.1130/L553.1.
- DeCelles, P. G., 2004, Late Jurassic to Eocene evolution of the Cordilleran thrust belt and foreland basin system, western U.S.A.: *American Journal of Science*, v. 304, p. 105, doi:10.2475/ajs.304.2.105.
- DeCelles, P.G., Ducea, M.N., Kapp, P., and Zandt, G., 2009, Cyclicity in Cordilleran orogenic systems: *Nature Geoscience*, v. 2, p. 251–257, doi:10.1038/ngeo469.
- Dickinson, W.R., 2004, Evolution of the North American Cordillera: *Annual Review of Earth and Planetary Sciences*, v. 32, p. 13–45, doi:10.1146/annurev.earth.32.101802.120257.
- Dodson, M.H., 1973, Closure temperature in cooling geochronological and petrological systems: *Contributions to Mineralogy and Petrology*, v. 40, p. 259–274, doi:10.1007/BF00373790.
- Dodson, A., Kennedy, B.M., and DePaolo, D.J., 1997, Helium and neon isotopes in the Innaha Basalt, Columbia River Basalt Group: Evidence for a Yellowstone plume source: *Earth and Planetary Science Letters*, v. 150, p. 443–451, doi:10.1016/S0012-821X(97)00090-3.
- Duke, G.I., 2009, Black Hills–Alberta carbonatite–kimberlite linear trend: Slab edge at depth? Interpreting the tectonic evolution of Pacific Rim margins using plate kinematics and slab window volcanism, v. 464, p. 186–194, doi:10.1016/j.tecto.2008.09.034.
- Dumitru, T.A., Elder, W.P., Hourigan, J.K., Chapman, A.D., Graham, S.A., and Wakabayashi, J., 2016, Four Cordilleran paleorivers that connected Sevier thrust zones in Idaho to depocenters in California, Washington, Wyoming, and, indirectly, Alaska: *Geology*, v. 44, p. 75–78, doi:10.1130/G37286.1.

- Dumitru, T.A., Ernst, W.G., Wright, J.E., Wooden, J.L., Wells, R.E., Farmer, L.P., Kent, A.J.R., and Graham, S.A., 2013, Eocene extension in Idaho generated massive sediment floods into the Franciscan trench and into the Tye, Great Valley, and Green River basins: *Geology*, v. 41, p. 187–190, doi:10.1130/G33746.1.
- Eddy, M.P., Clark, K.P., and Polenz, M., 2017, Age and volcanic stratigraphy of the Eocene Siletzia oceanic plateau in Washington and on Vancouver Island: *Lithosphere*, v. 9, p. 652–664, doi:10.1130/L650.1.
- Fayon, A.K., Tikoff, B., Kahn, M., and Gaschnig, R.M., 2017, Cooling and exhumation of the southern Idaho batholith: *Lithosphere*, v. 9, p. 299–314, doi:10.1130/L565.1.
- Flowers, R.M., Ketcham, R.A., Enkelmann, E., Gautheron, C., Reiners, P.W., Metcalf, J.R., Danišik, M., Stockli, D.F., and Brown, R.W., 2022a, (U-Th)/He chronology: Part 2. Considerations for evaluating, integrating, and interpreting conventional individual aliquot data: *GSA Bulletin*, v. 135, p. 137–161, doi:10.1130/B36268.1.
- Flowers, R.M., Zeitler, P.K., Danišik, M., Reiners, P.W., Gautheron, C., Ketcham, R.A., Metcalf, J.R., Stockli, D.F., Enkelmann, E., and Brown, R.W., 2022b, (U-Th)/He chronology: Part 1. Data, uncertainty, and reporting: *GSA Bulletin*, v. 135, p. 104–136, doi:10.1130/B36266.1.
- Foster, D.A., and Mark Fanning, C., 1997, Geochronology of the northern Idaho batholith and the Bitterroot metamorphic core complex: Magmatism preceding and contemporaneous with extension: *GSA Bulletin*, v. 109, p. 379–394, doi:10.1130/0016-7606(1997)109<0379:GOTNIB>2.3.CO;2.
- Foster, D.A., Schafer, C., Fanning, C.M., and Hyndman, D.W., 2001, Relationships between crustal partial melting, plutonism, orogeny, and exhumation: Idaho–Bitterroot batholith: *Partial Melting of Crust and Flow of Orogens*, v. 342, p. 313–350, doi:10.1016/S0040-1951(01)00169-X.
- Foster, D.A., and Raza, A., 2002, Low-temperature thermochronological record of exhumation of the Bitterroot metamorphic core complex, northern Cordilleran Orogen: *Low Temperature Thermochronology: From Tectonics to Landscape Evolution*, v. 349, p. 23–36, doi:10.1016/S0040-1951(02)00044-6.

- Fuentes, F., DeCelles, P.G., Constenius, K.N., and Gehrels, G.E., 2011, Evolution of the Cordilleran foreland basin system in northwestern Montana, U.S.A.: *GSA Bulletin*, v. 123, p. 507–533, doi:10.1130/B30204.1.
- Fuentes, F., DeCelles, P.G., and Constenius, K.N., 2012, Regional structure and kinematic history of the Cordilleran fold-thrust belt in northwestern Montana, USA: *Geosphere*, v. 8, p. 1104–1128, doi:10.1130/GES00773.1.
- Gallagher, K., 2012, Transdimensional inverse thermal history modeling for quantitative thermochronology: *Journal of Geophysical Research: Solid Earth*, v. 117, doi:10.1029/2011JB008825.
- Gaschnig, R.M., Vervoort, J.D., Lewis, R.S., and McClelland, W.C., 2010, Migrating magmatism in the northern US Cordillera: in situ U–Pb geochronology of the Idaho batholith: *Contributions to Mineralogy and Petrology*, v. 159, p. 863–883, doi:10.1007/s00410-009-0459-5.
- Gaschnig, R.M., Vervoort, J.D., Lewis, R.S., and Tikoff, B., 2011, Isotopic Evolution of the Idaho Batholith and Challis Intrusive Province, Northern US Cordillera: *Journal of Petrology*, v. 52, p. 2397–2429, doi:10.1093/petrology/egr050.
- Giorgis, S., McClelland, W., Fayon, A., Singer, B.S., and Tikoff, B., 2008, Timing of deformation and exhumation in the western Idaho shear zone, McCall, Idaho: *GSA Bulletin*, v. 120, p. 1119–1133, doi:10.1130/B26291.1.
- Giorgis, S., Tikoff, B., Kelso, P., and Markley, M., 2006, The role of material anisotropy in the neotectonic extension of the western Idaho shear zone, McCall, Idaho: *GSA Bulletin*, v. 118, p. 259–273, doi:10.1130/B25382.1.
- Gray, K.D., Isakson, V., Schwartz, D., and Vervoort, J.D., 2019, Orogenic link ~41°N–46°N: Collisional mountain building and basin closure in the Cordillera of western North America: *Geosphere*, v. 16, p. 136–181, doi:10.1130/GES02074.1.
- Grove, M., and Harrison, T.M., 1996, $^{40}\text{Ar}^*$ diffusion in Fe-rich biotite: *American Mineralogist*, v. 81, p. 940–951, doi:10.2138/am-1996-7-816.
- Grubbs, F.E., 1950, Sample Criteria for Testing Outlying Observations: *The Annals of Mathematical Statistics*, v. 21, p. 27–58, doi:10.1214/aoms/1177729885.

- Hales, T.C., Abt, D.L., Humphreys, E.D., and Roering, J.J., 2005, A lithospheric instability origin for Columbia River flood basalts and Wallowa Mountains uplift in northeast Oregon: *Nature*, v. 438, p. 842–845, doi:10.1038/nature04313.
- Hamilton, W.B., 1963, Metamorphism in the Riggins region, western Idaho: Professional Paper Report 436, doi:10.3133/pp436.
- Heller, P.L., Peterman, Z.E., O’Neil, J.R., and Shafiqullah, M., 1985, Isotopic provenance of sandstones from the Eocene Tyee Formation, Oregon Coast Range: *GSA Bulletin*, v. 96, p. 770–780, doi:10.1130/0016-7606(1985)96<770:IPOSFT>2.0.CO;2.
- Hiess, J., Condon, D.J., McLean, N., and Noble, S.R., 2012, 238U/235U Systematics in Terrestrial Uranium-Bearing Minerals: *Science*, v. 335, p. 1610–1614, doi:10.1126/science.1215507.
- Hooper, P.R., and Camp, V.E., 1981, Deformation of the southeast part of the Columbia Plateau: *Geology*, v. 9, p. 323–328, doi:10.1130/0091-7613(1981)9<323:DOTSPO>2.0.CO;2.
- Hooper, P.R., Camp, V.E., Reidel, S.P., and Ross, M.E., 2007, The origin of the Columbia River flood basalt province: Plume versus nonplume models, *in* Foulger, G.R. and Jurdy, D.M. eds., *Plates, Plumes and Planetary Processes*, Geological Society of America, v. 430, p. 0, doi:10.1130/2007.2430(30).
- Humphreys, E.D., 1995, Post-Laramide removal of the Farallon slab, western United States: *Geology*, v. 23, p. 987–990, doi:10.1130/0091-7613(1995)023<0987:PLROTF>2.3.CO;2.
- Janecke, S.U., 1992, Kinematics and timing of three superposed extensional systems, east central Idaho: Evidence for an Eocene tectonic transition: *Tectonics*, v. 11, p. 1121–1138, doi:10.1029/92TC00334.
- Kahn, M., Fayon, A.K., and Tikoff, B., 2020, Constraints on the post-orogenic tectonic history along the Salmon River suture zone from low-temperature thermochronology, western Idaho and eastern Oregon: *Rocky Mountain Geology*, v. 55, p. 27–54, doi:10.24872/rmgjournal.55.1.27.
- Kalin McDannell., 2022, QTQTPlot, <https://github.com/kmcdannell/QTQtPlot>

- Kasbohm, J., and Schoene, B. Rapid eruption of the Columbia River flood basalt and correlation with the mid-Miocene climate optimum: *Science Advances*, v. 4, p. eaat8223, doi:10.1126/sciadv.aat8223.
- Kent-Corson, M.L., Sherman, L.S., Mulch, A., and Chamberlain, C.P., 2006, Cenozoic topographic and climatic response to changing tectonic boundary conditions in Western North America: *Earth and Planetary Science Letters*, v. 252, p. 453–466, doi:10.1016/j.epsl.2006.09.049.
- Ketcham, R.A., 2005, Forward and Inverse Modeling of Low-Temperature Thermochronometry Data: *Reviews in Mineralogy and Geochemistry*, v. 58, p. 275–314, doi:10.2138/rmg.2005.58.11.
- Ketcham, R., Gautheron, C., and Tassan-Got, L., 2011, Accounting for long alpha-particle stopping distances in (U–Th–Sm)/He geochronology: Refinement of the baseline case: *Geochimica et Cosmochimica Acta*, v. 75, p. 7779–7791, doi:10.1016/j.gca.2011.10.011.
- Kiilsgaard, T.H., Stanford, L.R., and Lewis, R.S., 2001, Geologic Map of the Idaho City 30 x 60 Minute Quadrangle, Idaho: Idaho Geological Survey Map GM-29, scale: 1:100,000.
- Kiilsgaard, T.H., Stanford, L.R., and Lewis, R.S., 2006, Geologic Map of the Deadwood River 30 x 60 Minute Quadrangle, Idaho: Idaho Geological Survey Map GM-45, scale: 1:100,000.
- Kluyver, T. et al., 2016, Jupyter Notebooks - a publishing format for reproducible computational workflows, *in* Loizides, F. and Schmidt, B. eds., *Positioning and Power in Academic Publishing: Players, Agents and Agendas*, IOS Press, p. 87–90, <https://eprints.soton.ac.uk/403913/>.
- Kruckenberger, S.C., Whitney, D.L., Teyssier, C., Fanning, C.M., and Dunlap, W.J., 2008, Paleocene-Eocene migmatite crystallization, extension, and exhumation in the hinterland of the northern Cordillera: Okanogan dome, Washington, USA: *GSA Bulletin*, v. 120, p. 912–929, doi:10.1130/B26153.1.
- Larimer, J.E., Yanites, B.J., Phillips, W., and Mittelstaedt, E., 2019, Late Miocene rejuvenation of central Idaho landscape evolution: A case for surface processes driven by plume-lithosphere interaction: *Lithosphere*, v. 11, p. 59–72, doi:10.1130/L746.1.

- Lewis, R.S., and Kiilsgaard, T.H., 1991, Eocene plutonic rocks in south central Idaho: *Journal of Geophysical Research: Solid Earth*, v. 96, p. 13295–13311, doi:10.1029/91JB00601.
- Lewis, R.S., Link, P.K., Standford, L.R., and Long, S.P., 2012, Geologic map of Idaho: Idaho Geologic Survey, scale 1:750,000.
- Lindgren, W., 1904, A geological reconnaissance across the Bitterroot Range and Clearwater Mountains in Montana and Idaho: U.S. Geological Survey Professional Paper 27, 122 p, <https://doi.org/10.3133/pp27>.
- Martin, P.E., Metcalf, J.R., and Flowers, R.M., 2023, Calculation of uncertainty in the (U–Th)/He system: *Geochronology*, v. 5, p. 91–107, doi:10.5194/gchron-5-91-2023.
- McCaffrey, R., King, R.W., Payne, S.J., and Lancaster, M., 2013, Active tectonics of northwestern U.S. inferred from GPS-derived surface velocities: *Journal of Geophysical Research: Solid Earth*, v. 118, p. 709–723, doi:10.1029/2012JB009473.
- McKervey, J.A., 1998, The petrogenesis of the Eocene Challis Volcanic Group, Idaho, western U.S.A., PhD dissertation, The Open University (UK), 371 p, doi:10.21954/ou.ro.0000e215
- McPhillips, D., and Brandon, M.T., 2010, Using tracer thermochronology to measure modern relief change in the Sierra Nevada, California: *Earth and Planetary Science Letters*, v. 296, p. 373–383, doi:10.1016/j.epsl.2010.05.022.
- McQuarrie, N., and Rodgers, D.W., 1998, Subsidence of a volcanic basin by flexure and lower crustal flow: The eastern Snake River Plain, Idaho: *Tectonics*, v. 17, p. 203–220, doi:10.1029/97TC03762.
- Meyer, G.A., and Leidecker, M.E., 1999, Fluvial terraces along the Middle Fork Salmon River, Idaho, and their relation to glaciation, landslide dams, and incision rates: A preliminary analysis and river-mile guide, in Hughes, S.S., and Thackray, G.D., eds., *Guidebook to the Geology of Eastern Idaho: Pocatello, Idaho*, Idaho Museum of Natural History, p. 219–235.
- Mitchell, N.A., and Yanites, B.J., 2019, Spatially Variable Increase in Rock Uplift in the Northern U.S. Cordillera Recorded in the Distribution of River Knickpoints and Incision Depths: *Journal of Geophysical Research: Earth Surface*, v. 124, p. 1238–1260, doi:10.1029/2018JF004880.

- Moye, F.J., Hackett, W.R., Blakey, J.D., and Snider, L.G., 1988, Regional geologic setting and volcanic stratigraphy of the Challis volcanic field, central Idaho, in Link, P.K., and Hackett, W.R., eds., *Guidebook to the Geology of Central and Southern Idaho: Idaho Geological Survey Bulletin 27*, p. 87–97
- Murray, K.E., Orme, D.A., and Reiners, P.W., 2014, Effects of U–Th-rich grain boundary phases on apatite helium ages: *Chemical Geology*, v. 390, p. 135–151, doi:10.1016/j.chemgeo.2014.09.023.
- Norman, M.D., and Mertzman, S.A., 1991, Petrogenesis of Challis volcanics from central and southwestern Idaho: Trace element and Pb isotopic evidence: *Journal of Geophysical Research: Solid Earth*, v. 96, p. 13279–13293, doi:10.1029/91JB00285.
- Payne, S.J., McCaffrey, R., King, R.W., and Kattenhorn, S.A., 2012, A new interpretation of deformation rates in the Snake River Plain and adjacent basin and range regions based on GPS measurements: *Geophysical Journal International*, v. 189, p. 101–122, doi:10.1111/j.1365-246X.2012.05370.x.
- Pierce, K.L., and Morgan, L.A., 1992, Chapter 1: The track of the Yellowstone hot spot: Volcanism, faulting, and uplift, *in* Link, P.K., Kuntz, M.A., and Piatt, L.B. eds., *Regional Geology of Eastern Idaho and Western Wyoming*, Geological Society of America, v. 179, p. 0, doi:10.1130/MEM179-p1.
- QGIS Development Team, 2018, QGIS Geographic Information System, version 3.30.0 (‘s-Hertogenbosch’): Open Source Geospatial Foundation Project, <https://www.qgis.org/>.
- R Core Team, 2021, R: A language and environment for statistical computing: R Foundation for Statistical Computing, Vienna, Austria, <https://www.R-project.org/>.
- Reidel, S.P., Camp, V.E., Tolan, T.L., and Martin, B.S., 2013, The Columbia River flood basalt province: Stratigraphy, areal extent, volume, and physical volcanology, *in* Reidel, S.P., Camp, V.E., Ross, M.E., Wolff, J.A., Martin, B.S., Tolan, T.L., and Wells, R.E. eds., *The Columbia River Flood Basalt Province*, Geological Society of America, v. 497, p. 0, doi:10.1130/2013.2497(01).
- Ross, C.P., 1928, Mesozoic and Tertiary Granitic Rocks in Idaho: *The Journal of Geology*, v. 36, p. 673–693, doi:10.1086/623573.

- Roth, J.B., Fouch, M.J., James, D.E., and Carlson, R.W., 2008, Three-dimensional seismic velocity structure of the northwestern United States: *Geophysical Research Letters*, v. 35, doi:10.1029/2008GL034669.
- RStudio Team (2020). RStudio: Integrated Development for R. RStudio, PBC, Boston, MA
URL <http://www.rstudio.com/>.
- Ruppel, E.T., 1982, Cenozoic block uplifts in east-central Idaho and southwest Montana: U.S. Geological Survey Professional Paper 1224, 24 p.
- Saleeby, J.B., 1983, ACCRETIONARY TECTONICS OF THE NORTH AMERICAN CORDILLERA: *Annual Review of Earth and Planetary Sciences*, v. 11, p. 45–73, doi:10.1146/annurev.ea.11.050183.000401.
- Saleeby, J., Ducea, M., and Clemens-Knott, D., 2003, Production and loss of high-density batholithic root, southern Sierra Nevada, California: *Tectonics*, v. 22, doi:10.1029/2002TC001374.
- Sandford, R.F., and Snee, L.W., 2005, Geology and stratigraphy of the Challis Volcanic Group and related rocks, Little Wood River area, south-central Idaho: *Bulletin Report 2064II*, doi:10.3133/b2064II.
- Schildgen, T.F., Hodges, K.V., Whipple, K.X., Reiners, P.W., and Pringle, M.S., 2007, Uplift of the western margin of the Andean plateau revealed from canyon incision history, southern Peru: *Geology*, v. 35, p. 523, doi:10.1130/G23532A.1.
- Schmandt, B., and Humphreys, E., 2011, Seismically imaged relict slab from the 55 Ma Siletzia accretion to the northwest United States: *Geology*, v. 39, p. 175–178, doi:10.1130/G31558.1.
- Smith, R.B., 1978, 6: Seismicity, crustal structure, and intraplate tectonics of the interior of the western Cordillera, *in* Smith, R.B. and Eaton, G.P. eds., *Cenozoic Tectonics and Regional Geophysics of the Western Cordillera*, Geological Society of America, v. 152, p. 0, doi:10.1130/MEM152-p111.
- Spiegel, C., Kohn, B., Belton, D., Berner, Z., and Gleadow, A., 2009, Apatite (U–Th–Sm)/He thermochronology of rapidly cooled samples: The effect of He implantation: *Earth and Planetary Science Letters*, v. 285, p. 105–114, doi:10.1016/j.epsl.2009.05.045.
- Stanley, J., 2021, thermochronplotr: Make common plots in AHe thermochronology: R package version 0.1.0, <https://github.com/jstanley26/thermochronplotr>

- Suppe, J., Powell, C., and Berry, R., 1975, Regional topography, seismicity, Quaternary volcanism, and the present-day tectonics of the western United States: *American Journal of Science*, v. 275-A, p. 397–436.
- Sweetkind, D.S., and Blackwell, D.D., 1989, Fission-track evidence of the Cenozoic thermal history of the Idaho batholith: *Tectonophysics*, v. 157, p. 241–250, doi:10.1016/0040-1951(89)90142-X.
- Tian, Y., and Zhao, D., 2012, P-wave tomography of the western United States: Insight into the Yellowstone hotspot and the Juan de Fuca slab: *Physics of the Earth and Planetary Interiors*, v. 200–201, p. 72–84, doi:10.1016/j.pepi.2012.04.004.
- Tikoff, B., Kelso, P., Manduca, C., Markley, M.J., and Gillaspy, J., 2001, Lithospheric and crustal reactivation of an ancient plate boundary: the assembly and disassembly of the Salmon River suture zone, Idaho, USA, *in* Holdsworth, R.E., Strachan, R.A., Magloughlin, J.F., and Knipe, R.J. eds., *The Nature and Tectonic Significance of Fault Zone Weakening*, Geological Society of London, v. 186, p. 0, doi:10.1144/GSL.SP.2001.186.01.13.
- Turner, D., and Forbes, R., 1976, K-Ar studies in two deep basement drill holes: A new geologic estimate of argon blocking temperature for biotite: *Transactions-American Geophysical Union*, v. 57, p. 353–353.
- Umpleby, J.B., 1912, An Old Erosion Surface in Idaho: Its Age and Value as a Datum Plane: *The Journal of Geology*, v. 20, p. 139–147, doi:10.1086/621941.
- Vermeesch, P., and Tian, Y., 2014, Thermal history modelling: HeFTy vs. QTQt: *Earth-Science Reviews*, v. 139, p. 279–290, doi:10.1016/j.earscirev.2014.09.010.
- Vogl, J.J., Foster, D.A., Fanning, C.M., Kent, K.A., Rodgers, D.W., and Dienesch, T., 2012, Timing of extension in the Pioneer metamorphic core complex with implications for the spatial-temporal pattern of Cenozoic extension and exhumation in the northern U.S. Cordillera: *Tectonics*, v. 31, doi:10.1029/2011TC002981.
- Vogl, J.J., Min, K., Carmenate, A., Foster, D.A., and Marsellos, A., 2014, Miocene regional hotspot-related uplift, exhumation, and extension north of the Snake River Plain: Evidence from apatite (U-Th)/He thermochronology: *Lithosphere*, v. 6, p. 108–123, doi:10.1130/L308.1.

- Waschbusch, P.J., and McNutt, M.K., 1994, Yellowstone: A continental midplate (hot spot) swell: *Geophysical Research Letters*, v. 21, p. 1703–1706, doi:10.1029/94GL00429.
- Wells, R.E., 1989, Geologic map of the Cape Disappointment-Naselle River area, Pacific and Wahkiakum counties, Washington: IMAP Report 1832, doi:10.3133/i1832.
- Wetzel, K.F., and Stanley, J.R., 2022, Linking exhumation, paleo-relief, and rift formation to magmatic processes in the western Snake River Plain, Idaho, using apatite (U-Th)/He thermochronology: *Geosphere*, v. 18, p. 885–909, doi:10.1130/GES02453.1.
- Wickham, H., 2016, *ggplot2: Elegant graphics for data analysis*: New York, Springer-Verlag, <https://ggplot2.tidyverse.org>.
- Wickham, H., François, R., Henry, L., and Müller, K., 2021, *dplyr: A grammar of data manipulation: R package version 1.0.4*. <https://CRAN.R-project.org/package=dplyr>
- Wolf, R.A., Farley, K.A., and Kass, D.M., 1998, Modeling of the temperature sensitivity of the apatite (U–Th)/He thermochronometer: *Chemical Geology*, v. 148, p. 105–114, doi:10.1016/S0009-2541(98)00024-2.
- Wolfe, J.A., Forest, C.E., and Molnar, P., 1998, Paleobotanical evidence of Eocene and Oligocene paleoaltitudes in midlatitude western North America: *GSA Bulletin*, v. 110, p. 664–678, doi:10.1130/0016-7606(1998)110<0664:PEOEAO>2.3.CO;2.
- Wood, S., Clemens, D., Wood, S., and Clemens, D., 2002, Geologic and Tectonic History of the Western Snake River Plain, Idaho and Oregon: *Idaho Geological Survey Bulletin No. 30*, v. 30, p. 69–103.
- Yonkee, W.A., and Weil, A.B., 2015, Tectonic evolution of the Sevier and Laramide belts within the North American Cordillera orogenic system: *Earth-Science Reviews*, v. 150, p. 531–593, doi:10.1016/j.earscirev.2015.08.001.
- Zhou, Q., and Liu, L., 2019, Topographic evolution of the western United States since the early Miocene: *Earth and Planetary Science Letters*, v. 514, p. 1–12, doi:10.1016/j.epsl.2019.02.029.